# Mixing and switching

Dolk, V.S.

*Award date:*
2013

# Mixing and Switching

V.S. Dolk

CST 2013.075

Master's thesis

Coach(es): ir. M. Lauret

Supervisor: prof.dr.ir. W.P.M.H. Heemels

Eindhoven University of Technology
Department of Mechanical Engineering
Control Systems Technology

Eindhoven, August, 2013

August 12, 2013

## Summary

In this thesis the problem of efficient fluid mixing in the Stokes flow domain is tackled by means of optimal control from a switched systems perspective. In order to make the original infinite-dimensional problem tractable, temporal and spatial discretizations are used enabling us to regard the problem as the construction of an optimal schedule of sequence of discrete mixing actions. We exploit the cell-mapping method, an efficient and accurate computational tool for modeling and analyzing the system's behavior for a finite number of mixing actions. This modeling paradigm leads to a switched systems perspective that will be used to introduce a novel feedback law inspired by suboptimal rollout policies in dynamic programming contexts. By design this feedback law for mixing guarantees a performance improvement over any given periodic protocol. This new design methodology is validated both in simulation and experiments for the benchmark journal bearing flow.

# Acknowledgements

This thesis is the result of year work in the Hybrid Network Systems group, which would not be possible without contributions and help of many people.

In first place I would like to thank my supervisor Maurice Heemels and coaches Duarte Antunes and Menno Lauret for advising, coaching and mentoring me during this project. I could always count on you whenever I got stuck. Our meetings always led to useful and inspiring discussions which were full of novel ideas. Moreover, I learned a lot from your critical views on both the project itself as the paper which is definitely going to help me in my future career.

Next, I would like to thank Rob Hoogendijk and Ferry Schoenmakers. They helped me whenever I had struggles with getting the experimental setup running. Without their great knowledge about programming in C++ and the OpenCV library, I would never have managed to realize the experiments. I would also like to thank Patrick Anderson and Bram de Jager for being part of my MSc evaluation committee. In addition, I would like to thank the DCT-lab gang for a great work atmosphere and always enjoyable getaways. A special thanks to my girlfriend who, especially in the last stage of my MSc project, always kept me motivated to do the best I can do.

Finally, I would like to express here my warmest thanks to my family for all their support for the last twentyfive years.

Victor Dolk
August 2013

# Contents

# Part I
# Introduction

## Background

Mixing is a relevant topic since it is a widespread phenomena which occurs both in nature and industry. The focus of this study will be mixing of laminar flows. This is an important class within the field of mixing since turbulent flows, which often produce effective mixing, are not always achievable. Laminar flows are flows whose particle trajectories are characterized by parallel layers where there is no exchange between layers in contrast to turbulent flows whose particle trajectories in general show chaotic behavior [6]. Therefore, mixing in laminar flows is a challenging problem. The laminar flow type occurs in applications involving flows at small length scales, fluids with high viscosities and/or low speed flows.

Some examples in which mixing under laminar flow conditions plays an important role are polymer and food processing, pharmaceutics, biotechnology and microfluidics. Polymer and food-processing often involve high viscosity (non-Newtonian) substances like peanut butter and chocolate [14, 18]. In case of biotechnology often involve shear sensitive materials (like mammalian cells, plant cells, or mycelium) and therefore mixing must be achieved at low speeds. Microfluidics is a relatively new application field which concerns flow in devices having dimensions ranging from millimeters to micrometers and capable of handling volumes of fluid in the range of nano- to microliters ($10^{-9}$–$10^{-6}l$) [41]. In the last few years, the field of microfluidics is growing at a rapid pace due to the high number of areas which share interest in this new technology. An interesting example is, "lab-on-a-chip" devices which can be used for chemical analysis, environmental monitoring, medical diagnostics [32, 42, 59] and detecting bacteria in space [38]. The main advantages of the devices are portability, low fluid volumes, fast analysis and lower fabrication costs. In the near future, such devices will for example be deployed in order to improve global health due to the ability to diagnose infectious diseases. As explained by Yager *et al.* [42]:

> "The developing world does not have access to many of the best medical diagnostic technologies; they were designed for air-conditioned laboratories, refrigerated storage of chemicals, a constant supply of calibrators and reagents, stable electrical power, highly trained personnel and rapid transportation of samples. Microfluidic systems allow miniaturization and integration of complex functions, which could move sophisticated diagnostic tools out of the developed-world laboratory. These systems must be inexpensive, but also accurate, reliable, rugged and well suited to the medical and social contexts of the developing world."

This quote indicates the high importance of the field. However, in spite of the increasing performance and robustness for mixing that these new applications require, most industrial mixing processes are mainly based on trial-and-error and empiricism which yield great financial losses due to inefficient mixing processes [1, 18].

In the literature, several definitions of mixing exist. Paul *et al.* [18] defines mixing as the process of reducing inhomogeneity in order to achieve a desired result in which the homogeneity can represent a concentration, phase or temperature. A more mathematically rigorous definition of mixing is given in [55]; Consider a domain $\Omega$ and let $\Omega_\alpha, \Omega_\beta \subset \Omega$ denote any arbitrary regions in $\Omega$ and let $S$ denote a transformation under which $\Omega$ is invariant, *i.e.* $S(\Omega) = \Omega$. Furthermore let $\mu$ be the Lebesgue measure. Transformation $S$ is a mixing transformation if and only if

$$\frac{\mu(S^n(\Omega_\alpha) \cap \Omega_\beta)}{\mu(\Omega_\beta)} - \frac{\mu(\Omega_\alpha)}{\mu(\Omega)} \to 0 \text{ as } n \to \infty, \forall \Omega_\alpha, \Omega_\beta \subset \Omega. \tag{0.1}$$

The study to mixing started in the late 19th century. At this time, Reynolds already observed that repetition of stretching and folding, often referred as the *bakers transformation*, is an effective

mechanism for mixing in laminar flows [45]. However, foundations for mixing as a research topic were laid in the 1950s [51]. Only for the last few decades, research aims to find an unifying framework that describes the dynamics of laminar mixing processes. The principles of this unifying framework were laid down by Aref [5] who pointed out the link between mixing and chaos and introduced the term chaotic advection. Chaotic advection refers to the phenomena that even though a velocity field can be simple from an Eulerian perspective, the motion of the fluid particles can be chaotic in the Lagrangian sense [2, 49]. For more interesting work on this topic, see [9, 40, 55]. Traditional studies focus on time-periodic flows to induce chaos. However, periodic flows often yield unmixed regions which are called islands [34]. These island should be avoided in order to achieve effective mixing. Hence these studies aim to deduce conditions for which islands do not occur. Hereby, familiar analysis tools from the chaos and dynamical systems theory are used, for example the determination of periodic solutions [43, 19], Poincaré maps [50, 53] and the statistics of stretching which is related to the distribution of Lyapunov exponents [39, 44]. However, these conditions are flow specific in the sense that they have to be deduced on a case-by-case basis. Furthermore, most of these studies focus on asymptotic behavior of the system instead of short-time behavior which is relevant for rapid mixing.

Liu *et al.* [34] proposed the use of aperiodic flows for mixing since these are devoid of these periodic points and therefore islands do not occur. They observed that in general, mixing in periodic flows is worse than in aperiodic flows and concluded that much would be gained by achieving a better understanding of aperiodic mixing. This observation motivates the study of aperiodic mixing protocols and short-time behavior in particular. However several works has been devoted to designing such a protocol, see [1, 15, 13, 29, 34, 36, 27], no systematic methodology exists for designing feedback laws resulting in well-performing aperiodic mixing protocols.

## Objectives

This thesis has three main objectives:

- To obtain a mathematically tractable optimal control problem formulation.
- To propose a feedback control solution to this optimal control problem that outperforms any proposed periodic protocol over a finite horizon in particular satisfying computational constraints.
- To validate the proposed control solution both in simulation and experiment by means of the benchmark journal bearing flow.

## Outline thesis

The remainder of the report consists of three parts. Part II provides a paper which forms the main body of this thesis. This paper is organized as follows, in Section 2 we address the problem formulation. In Section 3 we take several steps to approximate this problem formulation in order to form a mathematically tractable optimal control problem. The control algorithm and controller design are elaborated on in Section 4. The benchmark system is discussed in Section 5 and results are presented of both simulations and experiments. Finally, in Section 6 we provide some concluding remarks. The paper focuses in particular on formulating an optimal control and proposing a feedback control solution for it. For this reason, Part III will provide some important additional concluding remarks based on work presented in the appendices. At last, the appendices are captured in Part IV which examines several aspects of the paper in more detail.

# Part II
# Paper: A switching feedback approach to optimize mixing of fluids

V.S. Dolk, M. Lauret, D.J. Antunes, P.D. Anderson and W.P.M.H. Heemels, in arbitrary order

**Abstract**

In this paper the problem of efficient fluid mixing in the Stokes flow domain is tackled by means of optimal control from a switched systems perspective. In order to make the original infinite-dimensional problem tractable, temporal and spatial discretizations are used enabling us to regard the problem as the construction of an optimal schedule of sequence of discrete mixing actions. We exploit the cell-mapping method, an efficient and accurate computational tool for modeling and analyzing the system's behavior for a finite number of mixing actions. This modeling paradigm leads to a switched systems perspective that will be used to introduce a novel feedback law inspired by suboptimal rollout policies in dynamic programming contexts. By design this feedback law for mixing guarantees a performance improvement over any given periodic protocol. This new design methodology is validated both in simulation and experiments for the benchmark journal bearing flow.

## 1 Introduction

Fluid mixing is a widespread process which occurs both in nature and in industry. Examples are polymer, chemical and food processing industries [14, 18]. In general, the goal of mixing is to homogenize a physical scalar entity which represents for example concentration or thermal energy, over a domain in order to increase homogeneity [51]. In many applications, flows are slow and/or very viscous (so-called Stokes flow) and therefore its velocity field structure is simple in comparison with turbulent flows. Due to the simplicity of the velocity field structure, mixing in Stokes flow regimes is highly non-trivial. As such, the design of an effective mixing mechanism dealing with this flow type is not only challenging but also practically relevant.

Achieving rapid mixing for Stokes flows is highly relevant for many applications including, large industrial mixing devices involving viscous fluids and compact and micro-scale mixing devices (a field of research known as microfluidics) where turbulence is absent. In particular, applications in microfluidics grow at fast pace due to the confluence of technologies and a number of fields that share an interest in this area [41]. An important application is for example the "lab-on-a-chip" concept which is used for chemical analysis, environmental monitoring, medical diagnostics [32, 42, 59] or detecting bacteria in space [38]. The main advantages of the devices are portability, low fluid volumes, fast analysis and lower fabrication costs. In the near future, such devices will for example be deployed in order to improve global health due to their ability to diagnose infectious diseases without the need of a state of the art laboratories.

Rapid mixing in Stokes flow regimes can be achieved by imposing time-varying boundary motions, pressure gradients and/or external body forces which lead to a time-varying velocity field. This idea arose from the fact that even though the velocity field is simple from an Eulerian perspective, the motion of the fluid particles can be chaotic in the Lagrangian sense [2, 49]. This process is known as chaotic advection, introduced by Aref [5], see also [9, 40, 55]. The specific time-varying mechanism in order to enhance mixing is called the mixing protocol. Conventionally such a protocol is designed in a time-periodic fashion leading to a periodic flow. However, periodic flows often yield unmixed regions which are called islands [34]. These island should be avoided in order to achieve effective mixing. Several methods are available for determining the existence of islands, e.g. the determination of periodic solutions [43, 19], Poincaré maps [50, 53], the statistics of stretching which is related to the distribution of Lyapunov exponents [39, 44] and spectral analysis via the mapping matrix formalism [49]. Traditional studies enhance mixing by realize certain conditions that guarantee the absence of islands. However, these conditions are flow specific in the sense that they have to be deduced on a

case-by-case basis. Furthermore, most of these studies focus on asymptotic behavior of the system instead of short-time behavior which is relevant for rapid mixing.

Aperiodic flows do not contain periodic points and therefore islands do not occur in these flows [34]. This observation motivates the study of aperiodic mixing protocols and short-time behavior in particular. As shown by example in [47, 29], a properly chosen aperiodic mixing protocol can indeed outperform time-periodic protocols. Such protocols are usually constructed *a priori* by means of empiricism and trial-and-error methods [34] and are implemented in an open loop fashion. However, recently several studies have been devoted to rigorously develop systematic methods to generate and control velocity fields in order to enhance mixing. To the best of the authors' knowledge, Aamo *et al.* [1] were the first to induce mixing by means of feedback control to generate an unstable flow. D'Alessandro *et al.* [15] and Hoeijmakers *et al.* [27] use an entropy approach to control the mixing behavior of a flow. These works only consider asymptotic properties of the controlled velocity fields and do not take into account the influence of different initial conditions. Mathew *et al.* [36], Cortelezzi *et al.* [12] and Couchman *et al.* [13] on the other hand aimed to optimize the velocity field based on the distribution of the physical scalar entity using a multiscale mixing measure [37]. However, none of these works provide theoretical performance guarantees and typically these works are not concerned with on-line implementability. *See Section B of the Appendices for a more extensive literature review on mixing control.*

The purpose of the present paper is to propose a *feedback* control solution that outperforms any proposed periodic protocol over a finite horizon. Our proposed solution is based on discretization of the mixing domain in both space and time, capturing the mixing behavior at discrete time $t_k$ by a vector $\mathbf{C}(t_k)$. Each component of $\mathbf{C}(t_k)$ indicates the average of the scalar entity to be mixed in a given region of the domain of interest. The cell-mapping method [25, 31, 47] is an efficient computational tool for predicting the fluid dynamics. This approach allows us to represent the system as a discrete-time linear time-variant system whose dynamics are described by the so-called mapping matrix. As the mapping matrix depends on a given control action and multiple control (mixing) actions are available, the overall dynamics of the mixing system can be captured by a *switched system* [33]. We can then regard the mixing protocol as the selection of a schedule consisting of a sequence of control options to be optimized in terms of a relevant mixing measure. Here, we focus on the so-called intensity of segregation [16] as an adequate measure for mixing although other options can also be used [37, 28]. Based on this modeling perspective on mixing, we propose a novel feedback control law for mixing inspired by suboptimal rollout policies in dynamic programming (DP) contexts [8]. It will be shown that online computations are feasible due to the sparsity of the mapping matrices and due to proposed modifications to the rollout algorithm. The methodology presented in this paper is not only suitable for closed-loop applications but can also straightforwardly be used for constructing aperiodic protocols *a priori*. Moreover, this paper is the first to propose a switching feedback approach for mixing optimization which includes performance improvements over periodic protocols.

In addition to providing a new modeling framework for mixing from a switched dynamical systems' perspective, and proposing a control solution for it, the proposed method is validated both in simulation as well as experiments. An experimental setup of the well-known journal bearing flow [10, 50, 54], *i.e.* the flow between two eccentric rotating cylinders, is used as a benchmark to show the effectiveness of the novel feedback methodology for optimized mixing.

The remainder of this paper is organized as follows. In Section 2 we address the problem formulation. In Section 3 we take several steps to obtain a relevant but tractable optimal control problem. The control algorithm and controller design are elaborated on in Section 4. The benchmark system is discussed in Section 5 and results are presented of both simulations and experiments. Finally, in Section 6 we provide some concluding remarks.

# 2 Problem formulation

In this paper we are concerned with achieving effective mixing using feedback control for two-dimensional incompressible slow or viscous flows, so-called Stokes flows. The Stokes flow regime is characterized by a small Reynolds number, i.e. $Re \ll 1$. This dimensionless number represents the ratio between

inertial and viscous forces and is given by

$$Re = \frac{V_{mean} L}{\nu}, \tag{2.1}$$

where $V_{mean}$ is the characteristic velocity scale, $L$ the characteristic length scale and $\nu$ the kinematic viscosity. Let $c(\mathbf{x}, t) \in [0, 1] \subset \mathbb{R}$ be a normalized positive scalar quantity in a domain $\Omega \subset \mathbb{R}^2$ associated with a transported physical entity (for example thermal energy or concentration) which is preserved, i.e. the surface integral $\int_\Omega c(\mathbf{x}, t) dA$ remains constant, where $\mathbf{x} = (x, y)^\top \in \Omega$ are Cartesian coordinates, $t \in \mathbb{R}^+$ denotes the time and $dA$ an appropriate area measure. The scalar quantity $c : \Omega \times \mathbb{R}^+ \to [0, 1]$ evolves according to the diffusion advection equation [6]. Complete mixing in the domain $\Omega$ is achieved at time $t$ when the scalar quantity is distributed homogeneously over the entire domain, i.e. $c(\mathbf{x}, t) = \overline{c} = \int_\Omega c(\mathbf{x}, t) dA / A_\Omega$, for all $\mathbf{x} \in \Omega$, where $\overline{c}$ is the average of $c(\mathbf{x}, t)$ over $\Omega$ and $A_\Omega = \int_\Omega dA$ the area of domain $\Omega$. The rate of homogenization of $c(\mathbf{x}, t)$ in Stokes flows can be enhanced by an actuator mechanism imposing time-varying boundary motions, pressure gradients and/or body forces, referred as mixing actions. For example, the actuator mechanism of the journal bearing setup described in Section 5.1, consists of imposing boundary motions, namely rotating the inner and/or outer cylinder. *See Section A of the Appendices for a more detailed problem description from a fluid dynamics point of view.*

From a high level point of view, the problem tackled in the present paper is the question of how to systematically design a mixing protocol determining the mixing actions over time, either *a priori* or in closed loop by means of an on-line computed mixing policy whereby depending on the mixing context, one can have different objectives. An objective could be (i) to obtain the best mixing performance within a certain time frame according to a specific mixing measure; (ii) to improve transitory mixing behavior over a given time horizon; or (iii) to improve asymptotic mixing behavior. In the next sections, we will provide a general modeling, analysis and design framework for formalizing and addressing the mentioned optimal control problem that allows for different objectives and definitions of mixing efficiency and mixing quality.

# 3 Modeling and performance analysis framework

Obtaining a mathematical formulation of the high-level control problem provided in the previous section might be tedious. In addition, even if such a formulation would be obtained, it would be intractable due to the infinite-dimensional character of the problem. Therefore, we discuss in this section a mathematical control problem that forms an accurate approximation of the high-level problem formulation, whose solution will be close to practical implementation. To obtain this mathematical formulation, three main steps are taken. First, the domain is partitioned into a finite number of cells. Secondly, the mixing process is sampled at discrete time instants $t_k = k\Delta t$, $k \in \mathbb{N}$. At last, we restrict ourselves to a mixing protocol which is built up as a sequence consisting of control inputs, referred to as mixing actions, which are selected from a finite set $\mathcal{M} = \{1, 2, \ldots, M\}$ with $M$ the number of available mixing actions. A mixing action $m \in \mathcal{M}$ is a pre-defined actuator mechanism over the finite time window $\Delta t$. In the journal bearing setup for example, a mixing action is to rotate the inner and/or outer cylinder a specific angle $\theta$ in the finite time window $\Delta t$. Hence, the mixing protocol $\sigma$ is a sequence of length $k_F$, where $k_F = T_f / \Delta t$ and $T_f$ the duration of the mixing process, consisting of scheduling variables each corresponding to a certain mixing action, i.e. $\sigma : \{0, 1, \ldots, k_F - 1\} \to \mathcal{M}$. To achieve these three steps, we will exploit the cell-mapping method as explained in Section 3.1. In the first part of this section, we discuss the cell-mapping method. This will lead to a discrete-time linear switched system model of the mixing process. This novel perspective on mixing will be instrumental for our optimal mixing strategy. After that, Section 3.2 addresses the quantification of the mixing performance. At last in Section 3.3, the provided modeling framework and performance measure are used to formulate an optimal control problem, whose (approximate) solution shall lead to the model-based feedback control solution presented in Section 4.

## 3.1 Discretization using the cell-mapping method

The cell-mapping method, introduced in [31], is an efficient computational tool to investigate the influence of different mixing protocols on overall mixing quality at a feasible computational cost. It provides a description of the transport of the scalar quantity $c(\mathbf{x}, t)$ after a discrete time step $\Delta t$ given a certain mixing action, in a domain $\Omega$ over a grid of $N$ cells $\Omega_i$, where $i \in \{1, 2, \ldots, N\}$. The cells $\{\Omega_1, \Omega_2, \ldots, \Omega_N\}$ form a partition of $\Omega$ in the sense that $\bigcup_{i=1}^{N} \Omega_i = \Omega$ and that all cells are disjoint, i.e. $\Omega_i \cap \Omega_j = \emptyset$ when $i \neq j$. The method will lead to a mapping matrix $\Phi$ of which the elements define the fraction of material being transported from one cell to another in time span $\Delta t$, as we will discuss below.

A computationally efficient method to compute the elements of a mapping matrix $\Phi_m$, is by tracking $P$ individual discrete particles. The path of a single particle is determined by the solution of

$$\dot{\mathbf{x}} = \mathbf{v}(\mathbf{x}, m, t) \tag{3.1}$$

$$\mathbf{x}(0) = \mathbf{x}_0 \tag{3.2}$$

where $\mathbf{v} : \mathbb{R}^2 \times \mathcal{M} \times \mathbb{R}^+ \to \mathbb{R}^2$ is the system's velocity field, $m \in \mathcal{M}$ the mixing action and $\mathbf{x}_0$ the initial condition of the particle. This velocity field can either be found analytically or numerically by means of the Navier-Stokes equations [6] and the imposed boundary conditions. The solution to these equations depends on boundary motions, pressure gradients and/or body forces, i.e. the mixing actions. Therefore, each mixing action $m \in \mathcal{M}$ yields a different velocity field (3.1) and thus for each $m \in \mathcal{M}$ a mapping matrix has to be computed. Under the assumptions that transient dynamics and surface tensions are negligible, the dynamics of the system given by (3.1) only depends on the present state, i.e. no hysteresis phenomena occur. The entries of the mapping matrix $\mathbf{\Phi}_m$ are then determined by

$$\Phi_{m,ij} = \frac{p_{ij}}{p_j}, \tag{3.3}$$

where $p_j$ is the amount of particles in donor cell $\Omega_j$ at $t = t_0 = 0$ and $p_{ij}$ is the amount of particles traveled from donor cell $\Omega_j$ to recipient cell $\Omega_i$ at $t_1 = t_0 + \Delta t$ (shown in Figure 3.1). The preservation property of $c(\mathbf{x}, t)$, implies that $\sum_{i=1}^{n} \Phi_{m,ij} = 1$ for each $j \in \{1, 2, \ldots, N\}$. Note that the size of the mapping matrix is equal to $N \times N$. Furthermore, since $0 \leq p_{ij} \leq p_j$, the values $\Phi_{ij}$ are restricted to the interval $[0, 1]$ for all $i, j \in \{1, 2, \ldots, N\}$.

The mapping matrix $\Phi_m$ can be used to determine the transport of the scalar quantity $c(\mathbf{x}, t)$ over the domain $\Omega$ over a grid of $N$ cells after discrete time step $\Delta t$ via a linear matrix multiplication as presented next. Let $C_i(t)$ be the averaged quantity in each cell $\Omega_i$ at time $t$, i.e.

$$C_i(t) = \frac{\int_{\Omega_i} c(\mathbf{x}, t) dA}{A_{\Omega_i}}, \tag{3.4}$$

where $A_{\Omega_i} = \int_{\Omega_i} dA$ the area of domain $\Omega_i$. Hence, $C_i(t) \in [0, 1]$ for $i \in \{1, 2, \ldots, N\}$ and let $\mathbf{C}(t)$ be the column of averaged concentrations

$$\mathbf{C}(t) = \begin{bmatrix} C_1(t) \\ \vdots \\ C_N(t) \end{bmatrix}. \tag{3.5}$$

The mapping matrix $\mathbf{\Phi}_m$ maps $\mathbf{C}(t_k)$ to $\mathbf{C}(t_{k+1})$ according to

$$\mathbf{C}(t_{k+1}) = \mathbf{\Phi}_m \mathbf{C}(t_k), \tag{3.6}$$

for all $k \in \mathbb{N}$, where $t_k = k\Delta t$ and $m$ is the chosen mixing action.

When using mapping matrices, important issues are how to choose the length of the time steps $\Delta t$ and as well the number of cells $N$ since both $\Delta t$ and $N$ are involved in the trade-off between accuracy and computational complexity. The discretization of mixing domain $\Omega$ requires sub-domain averaging as shown in (3.4). For this reason, the method can not capture sub-domain features. This results in

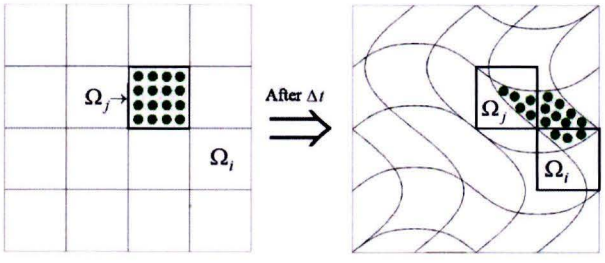


Figure 3.1: Computation of the mapping matrix from redistribution of material over a grid of finite mapping cells: discrete particle-based approach [49].

a numerical error known as numerical diffusion. Choosing a large number of cells $N$ mitigates this numerical error but the growth of the mapping matrix might be impractical from a computational point of view. However, on the other hand in practice diffusion is always present and hence this numerical error does not necessarily degrade the accuracy of the mapping [23, 24, 31]. Despite of this fact, the number of cells $N$ is typically large for many applications. Hence, one has to exploit the sparsity property the mapping matrix since sparser mapping matrices are from a computational point of view easier to handle, both in terms of number of operations to *e.g.* multiply such matrices and in terms of memory needed to store them. This important sparsity property is obtained when the mapping matrix is computed over a relatively small time step $\Delta t$. The reason for this sparsity is that the fluid from an arbitrary donor domain $\Omega_j$ will only be distributed over a small subset of the entire domain $\Omega$ in a short time span. Hence, $m_{ij} = 0$ for a majority of pairs $(i, j) \in \{1, 2, \ldots, N\}^2$, which corresponds to zero elements in the mapping matrix. Clearly, smaller time steps will lead to sparser mapping matrices. One important drawback however, is that every time step introduces a numerical error. Hence, a good balance of $N$ and $\Delta t$ is needed, see [31, 23] for a more detailed discussion on these choices. *See Section E of the Appendices for a discussion on how to choose the mapping grid with respect to diffusivity and control.*

**Remark** In this work, the mapping matrices are derived for pure advective flows. However, Gorodetrskyi *et al.* [23, 24] show that molecular diffusion can be included into the mapping matrix formalism as well. As a consequence, the approach presented in this paper also applies in that case.

As already mentioned, the cell-mapping method leads to different mapping matrices for each mixing action. Since at each discrete time step $t_k = k\Delta t$ a new mixing action, $\sigma_k \in \mathcal{M}$, will be chosen, the system can be described as a linear discrete-time switched system. To do so, we will use as the state vector of the system

$$\mathbf{e}_k \quad := \quad \mathbf{C}(t_k) - \bar{c}\mathbf{1}, \tag{3.7}$$

representing the error between the current state and the homogeneous state $\bar{c}\mathbf{1}$ at time $t_k = k\Delta t$, $k \in \mathbb{N}$ where $\bar{c} = \int_\Omega c(\mathbf{x}, t)dA/A_\Omega$. The system's model then becomes

$$\mathbf{e}_{k+1} = \Phi_{\sigma_k}\mathbf{e}_k, \tag{3.8}$$

where $\Phi_{\sigma_k}$ is the system matrix which depends on the mixing action or control input $\sigma_k \in \mathcal{M}, k \in \mathbb{N}$. Hence, by choosing this setup, the system dynamics are reduced to the switched system (3.8) and the mixing protocol has to determine the sequence $\sigma = (\sigma_0, \ldots, \sigma_{k_F-1})$. The only ingredient left to be defined is an appropriate measure for quantifying mixing performance.

## 3.2 Quantifying mixing performance

In the literature, several measures are used to quantify mixing performance depending on the focus of the study. Performance measures are, for instance, the striation thickness and the length of stretch

which quantify the deformation of a material element, and the scale of segregation, intensity of segregation [28] and the Mix-Norm [37], which quantify the inhomogeneity of the scalar field to be mixed. For this research, the intensity of segregation is chosen for quantifying mixing performance. Yet it is important to mention that the control methods to be presented later on can be adapted to other mixing measures in a straightforward manner.

As mentioned before, the objective of mixing is to reach the equilibrium in which the scalar quantity $c(\mathbf{x}, t)$ is homogeneous over the entire domain, i.e. $c(\mathbf{x}, t) = \bar{c}$, for all $\mathbf{x} \in \Omega$. The intensity of segregation represents the variance of the quantity $c(\mathbf{x}, t)$ with respect to the equilibrium value $\bar{c}$. The variance is equal to the squared deviation $\sigma_c$, which is the normalized $\mathcal{L}_2$-norm of the error $c(\mathbf{x}, t) - \bar{c}$ given by

$$\sigma_c(t) = \frac{\|c(\mathbf{x}, t) - \bar{c}\|_{\mathcal{L}_2}}{\sqrt{A_\Omega}}, \tag{3.9}$$

where $\|f(\mathbf{x})\|_{\mathcal{L}_2} = \left(\int_\Omega |f(\mathbf{x})|^2 dA\right)^{\frac{1}{2}}$. The intensity of segregation [16, 31] is defined as

$$I(t) = \frac{\sigma_c(t)^2}{\bar{c}(1-\bar{c})}. \tag{3.10}$$

The denominator is chosen such that $I(t) \in [0, 1]$, for all $t \in \mathbb{R}^+$. The intensity of segregation defined in discrete form is given by

$$I_d(t) = \frac{1}{A_\Omega} \sum_{i=1}^{N} \frac{(C_i(t) - \bar{c})^2}{\bar{c}(1-\bar{c})} A_{\Omega_i}, \tag{3.11}$$

where $C_i(t) = \int_{\Omega_i} c(\mathbf{x}, t) dA / A_{\Omega_i}$ as defined before in (3.4). In the worst case, $C_i(t)$ is either one or zero for all $i \in \{1, 2, \ldots, N\}$ which yields an intensity of segregation equal to one. The ideal case, $C_i(t) = \bar{c}$ for all $i \in \{1, 2, \ldots, N\}$ corresponds to $I_d(t) = 0$.

An important observation is that the value of $I_d(t)$ depends on the choices for the subdomains $\Omega_1, \Omega_2, \ldots, \Omega_N$. Therefore, the intensity of segregation is only a comparable measure if the same grid is used. The cell partitioning is often chosen equal to the partitioning used for the mapping method since it corresponds to the length scale of interest such that critical striation sizes are visible. The intensity of segregation $I_d(t)$ at time $t = t_k = t_0 + k\Delta t$ in terms of the state (3.7) is given by

$$I_d(t) = I_d(\mathbf{e}_k) = \mathbf{e}_k^\top Q \mathbf{e}_k, \tag{3.12}$$

where $Q$ is a diagonal matrix where $Q_{ii} = \frac{A_{\Omega_i}}{A_\Omega \bar{c}(1-\bar{c})}$ and $Q_{ij} = 0$ if $j \neq i$, $i, j \in \{1, \ldots, N\}$. With some abuse of notation, we write $I_d(\mathbf{e}_k)$ for $I_d(t_k)$. Now, the switched system perspective (3.8) and the mixing measure (3.12) are provided, the high-level problem formulation given in Section 2 can be approximated by a mathematically tractable problem formulation presented next.

## 3.3 Optimization problem

Taking into account the system description (3.8) and the intensity of segregation (3.12), we define the cost $g : [0, 1]^N \times \mathcal{M} \to \mathbb{R}^+$ given by

$$g(\mathbf{e}) = I_d(\mathbf{e}) \tag{3.13}$$
$$= \mathbf{e}^\top Q \mathbf{e}. \tag{3.14}$$

Depending on the mixing context, one can have different objectives, including for instance,

Objective 1 : Achieve the best mixing performance, measured by intensity of segregation at a certain terminal time $t_{k_F}$.

Objective 2 : Improve transitory mixing behavior in terms of a cumulative cost over a given time horizon $\{0, 1, \ldots, k_F\}$.

Objective 3 : Optimize the mixing behavior in terms of a cumulative discounted cost over an infinite horizon if one is interested in asymptotic behavior.

A cost-function which can capture all these objectives is

$$J_\sigma(\mathbf{e}_0) = \sum_{l=0}^{\infty} \beta_l g(\mathbf{e}_l), \tag{3.15}$$

where $\sigma$ denotes the mixing schedule and$\beta_l$, $l \in \mathbb{N}$ are tuning parameters which can be chosen in accordance with the mixing context. Determining the cost function given by (3.15) from a computational point of view, will be addressed in the next section. In fact, the choice for $\beta_l$, $l \in \mathbb{N}$ corresponding to the first three objectives, is as follows:

Objective 1 $\beta_l = \begin{cases} 1 & \text{if } l = k_F \\ 0 & \text{otherwise} \end{cases}$

Objective 2 $\beta_l = \begin{cases} w_l & \text{if } 0 \leq l \leq k_F, \text{ where } w_l \text{are weighting factors} \\ 0 & \text{otherwise} \end{cases}$

Objective 3 $\beta_l = \alpha^l$, $l \in \mathbb{N}$, where $0 < \alpha \leq 1$ is a discount factor allowing to properly specify the importance of transitory and asymptotic behavior in a specific problem.

Hence, the optimization problem now becomes:

$$J^*(\mathbf{e}_0) = \min_{\sigma \in \mathcal{M}^\infty} J_\sigma(\mathbf{e}_0) \tag{3.16}$$

subject to (3.8), and find an optimal sequence $\pi^*(\mathbf{e}_0)$, *i.e.*

$$\pi^*(\mathbf{e}_0) = \arg \min_{\sigma \in \mathcal{M}^\infty} J_\sigma(\mathbf{e}_0), \tag{3.17}$$

where $\pi : [0,1]^N \to \mathcal{M}^\infty$ denotes a mixing policy which maps a state $\mathbf{e}$ to a mixing sequence $\sigma : \mathbb{N} \to \mathcal{M}$.

**Remark** The control effort can be taken into consideration by defining the cost $g$ as,

$$g(\mathbf{e}, m) = \mathbf{e}^\top Q \mathbf{e} + R(m)$$

where the first term penalizes the mixture variance and the second term the control effort. The control effort term $R(m)$ maps the discrete set of mixing actions $\mathcal{M}$ to the energy involved in the corresponding mixing action. In addition, the optimal control problem (3.17) can be subjected to constraints regarding control effort. In this work, we focus on short-term mixing behavior where we disregard control effort issues. However, the machinery presented below can be applied *mutatis mutandis* to the other cases as well.

The optimal control problem (3.16) and (3.17) subject to (3.8) can be solved *a priori*, where the optimal protocol $\pi^{k,*}(\mathbf{e}_0)$ is implemented in open loop. However, a feedback implementation based on Bellman's optimality principle [7] yields a policy less sensitive to modeling and measurement uncertainties. In the latter case, the optimal sequence $\pi^*(\mathbf{e}_0)$ is determined on-line according to

$$J_{\sigma^k}(\mathbf{e}_k) = \sum_{l=k}^{\infty} \beta_l g(\mathbf{e}_l) \tag{3.18}$$

$$\pi^*(\mathbf{e}_k) = \arg \min_{\sigma^k \in \mathcal{I}_{full,k}} J_{\sigma^k}(\mathbf{e}_k), \tag{3.19}$$

subject to (3.8), for each time step $t_k$ where $k \in \{0, 1, \ldots, k_F - 1\}$. The applied control input at discrete time $t_k$ is taken as the first entry of the sequence $\pi^*(\mathbf{e}_k)$, *i.e.* $\sigma_k^*$ where $\sigma^* = \pi^*(\mathbf{e}_k)$. Thus in closed

loop, the optimization is repeated at each time step using the current measured state which makes the policy less sensitive to modeling and measurement uncertainties.

Important to notice is that for the first two objectives, it is only necessary to consider a finite horizon which means a finite decision set $\mathcal{M}^{k_F-k}$ can be considered in (3.17) in order to obtain a policy which returns a finite mixing protocol, *i.e.* $\pi^*(\mathbf{e}_0) \in \mathcal{M}^{k_F}$. Furthermore, notice that these two objectives yield a time-varying policy contrary to the third objective in which the optimal policy is time-invariant (see [8]). Since the aim of this paper is to optimize mixing over a finite horizon in which asymptotic behavior is irrelevant, we disregard the third objective.

Finding the optimal numerical solution to (3.16) and (3.17) is often computationally expensive due to combinational nature of the decision set $\mathcal{I}_{\text{full}}$ which is growing exponentially with the length of the horizon $k_F$. This is the well-known curse of dimensionality of DP [8]. Since we aim to construct a feedback control method using only restricted computation time, we propose a suboptimal strategy to approximate the solution given by (3.17) while still guaranteeing important closed-loop properties.

# 4 Proposed feedback mixing method

In this section, we use the optimal control framework presented in the previous section to propose a computationally tractable control method inspired by a suboptimal method for dynamic programming (DP) [8]. In addition, we discuss how to implement this control approach on-line within computational constraints.

In general, optimal control problems for switched systems are difficult to solve. In the literature, stabilizing suboptimal feedback policies were derived from S-procedure stability conditions [46, Ch.2] and Lyapunov stability conditions [33, Ch.3.4] see, *i.e.* *[26, 35]*, $\epsilon$-relaxation policies [57, 56, 58] and rollout policies [3, 4, 8]. For more work about discrete switching control, see also [17, 21, 22]. Most of these approaches are LMI-based which are for this particular application, due to the relatively large size of the mapping matrices, computationally intractable in spite of recently developed numerical techniques [30, 52].

Several works in the field of mixing [12, 29, 34], proposed the following simple computational efficient policy which we shall call minimum error first (MEF): Choose $\sigma_k$ at time $t_k$ that yields the best performance at the next time step $t_{k+1}$ (in our case in terms of the intensity of segregation), *i.e.*

$$\sigma_k = \min_{m \in \mathcal{M}} g(\Phi_m \mathbf{e}_k). \tag{4.1}$$

Since this policy only requires one step ahead predictions, the computational effort is low. However, only asymptotic performance guarantees could be derived by means of the S-procedure, in a similar fashion to the arguments presented in [46, Ch.2]. For a finite horizon, it is unclear what this policy has to offer since asymptotic properties do not yield direct quantitative information about mixing efficiency over a finite horizon [12] and thus does not always outperform periodic protocols as we will show in Section 5.2.

For these two reasons, we focus on a method to approximately solve the optimal control problem (3.17) that is able to deal with large matrices and in addition that can provide guarantees of outperforming available periodic mixing solutions. Due to the latter aspect, performance guarantees are immediately obtained. To do so, we will use so-called roll-out policies (see [3, 4, 8, Ch. 6]).

The proposed closed-loop rollout policy uses some known base policy in order to obtain an approximate solution to (3.19) by restricting the number of decisions beyond a certain horizon (without sacrificing the overall freedom in the schedules). To explain in more detail, instead of optimizing the entire sequence $\sigma^k$ for each time step $t_k$, only the first $H$, $0 \leq H < k_F - l$ schedule variables

$$\sigma_k, \sigma_{k+1}, \ldots, \sigma_{k+H-1}, \tag{4.2}$$

known as the lookahead horizon, are chosen to be free and being optimized while

$$\sigma_{k+H}, \sigma_{k+H+1}, \ldots, \sigma_{k_F-1}, \tag{4.3}$$

are fixed and chosen according to a base policy $\pi_{\text{base}}$. Thereby, the decision set has been reduced $\mathcal{I}_{\text{roll-out},k} \subset \mathcal{I}_{\text{full},k}$, in other words the amount of protocols to be examined is equal to $m^H$ instead of $m^{k_F}$ in case of $\mathcal{I}_{\text{full},k}$. Analogously to the optimal policy given in (3.19), the rollout policy is given by

$$\pi^{k,\text{roll-out}}(\mathbf{e}_k) = \arg \min_{\sigma^k \in \mathcal{I}_{\text{roll-out},k}} J_{\sigma^k}(\mathbf{e}_k), \tag{4.4}$$

for all $k \in \{0, 1, \ldots, k_F - 1\}$. The rollout policy always outperforms the corresponding base policy as stated in the following theorem.

**Theorem 1** [8, Ch. 6.4]: *Let $J_{\pi^k,\text{rollout}}(\mathbf{e}) = \min_{\sigma^k \in \mathcal{I}_{\text{rollout},k}} J_{\sigma^k}(\mathbf{e})$, where $\mathcal{I}_{\text{rollout},k}$ is a set containing all protocols satisfying (4.2) and (4.3), and let $J_{\pi^k,\text{base}}(\mathbf{e}) = J_{\sigma^k,\text{base}}(\mathbf{e})$ be the costs-to-go of the roll-out and base policy respectively, then*

$$J_{\pi^k,\text{rollout}}(\mathbf{e}) \leq J_{\pi^k,\text{base}}(\mathbf{e}) \tag{4.5}$$

*for all $k \in \{0, 1, \ldots, k_F - 1\}$ and every state $\mathbf{e}$ as long as $\sigma^{k,\text{base}} \in \mathcal{I}_k$.*

□

By choosing the base policy as an available periodic mixing sequence, it will be guaranteed that the rollout strategy will never perform worse than this periodic solution over an arbitrary finite horizon. The periodic protocol $\sigma^{\text{periodic}}$ consists of a repeating set of $K$ schedule variables denoted by

$$v = (v_0, v_1, \ldots, v_{K-1}),$$

where $v_i \in \mathcal{M}$, $i \in \{0, 1, \ldots K - 1\}$. Hence, for protocol $\sigma^{\text{periodic}}$ we have

$$\sigma_0^{\text{periodic}} = v_0, \sigma_1^{\text{periodic}} = v_1, \ldots, \sigma_{K-1}^{\text{periodic}} = v_{K-1}$$

and

$$\sigma_{k+K}^{\text{periodic}} = \sigma_k^{\text{periodic}} \text{ for all } k \in \{0, 1, \ldots, k_F - K\}.$$

The periodic protocol does not have to be optimal in order to obtain an effective rollout policy as we will show in Section 5. However, the choice of a well-performing base policy is in general beneficial for the rollout algorithm due to the performance guarantee given by Theorem 1.

The rollout algorithm can be made computationally more efficient by means of pruning. Instead of determining the cost $J_{\sigma^k}(\mathbf{x})$ for each $\sigma^k \in \mathcal{I}_{\text{rollout},k}$, only a subset with promising options is being evaluated. This manifests as follows the cost is computed for each $\sigma^k \in \mathcal{I}_{\text{rollout},k}$ up until $k_{\min}$ instead of $k_F$, where $k_{\min} < k_F$:

$$J_{\sigma^k}^{\min}(\mathbf{e}) = \sum_{l=k}^{k_{\min}} \beta_{\min,l} g(\mathbf{e}_l), \tag{4.6}$$

where $\beta_{\min,l}$, $l \in \mathbb{N}$ are tuning parameters which can be chosen in accordance with the mixing context. Note that parameters $\beta_{\min,l}$, $l \in \mathbb{N}$ can be chosen different from $\beta_l$, $l \in \mathbb{N}$ used in (3.15) and (3.18). Based on this cost, the best $n_{\min}$ options are chosen to be evaluated over the entire horizon $k_F$. This pruning approach reduces the maximum amount of required matrix multiplications per time step from $m^H(k_F - 1)$ to $m^H k_{\min} + n_{\min}(k_F - 1 - k_{\min})$. Important to note is that the base policy must be evaluated over the entire horizon as well in order to maintain the performance guarantee given by Theorem 1. Moreover, notice that in general larger $k_{\min}$ and $n_{\min}$ will yield better performance, since a larger $k_{\min}$ will better reveal promising options and a larger $n_{\min}$ implies that more options will be evaluated. Consequently, if $k_{\min}$ and $n_{\min}$ are chosen sufficiently large, the performance will not degrade at all, with respect to the algorithm without pruning.

So far, we considered the rollout algorithm in order to optimize the cost function (3.15). However, how to compute such a cost function has not been addressed. For $\sigma \in \mathcal{M}^{k_F}$, let $\Xi_\sigma(k_2, k_1) := \Phi_{\sigma_{k_2}} \Phi_{\sigma_{k_2-1}} \ldots \Phi_{\sigma_{k_1+1}} \Phi_{\sigma_{k_1}}$ where $k_2 \geq k_1$ and $k_1, k_2 \in \{0, 1, \ldots, k_F - 1\}$, then (3.8) leads to

$$\mathbf{e}_{k_2} = \Xi_\sigma(k_2, k_1) \mathbf{e}_{k_1}. \tag{4.7}$$

**Algorithm 1** Determine $J_l(\mathbf{x}, \sigma)$ step-by-step

Set $J_{\sigma^k}(\mathbf{x}) = 0$
**for** each $l \in \{k, k+1, \ldots, k_F - 1\}$
  $J_{\sigma^k}(\mathbf{x}) = J_{\sigma^k}(\mathbf{x}) + \beta_l I_d(\mathbf{x})$
  $\mathbf{x} = A_{\sigma_l}\mathbf{x}$
**end for**
Return $J_{\sigma^k}(\mathbf{x})$

**Algorithm 2** Rollout policy using one step ahead prediction

Execute pre-defined initial action $\sigma_0$ at time $t = t_0$
**for** each $k \in \{0, 1, \ldots, k_F - 1\}$
  Measure $\mathbf{x}_k$ (at time $t_k$)
  Predict next state $\tilde{\mathbf{x}}_{k+1} = A_{\sigma_k}\mathbf{x}_k$.
  **for** each $\sigma \in \mathcal{I}_{roll-out,k+1}$
    Compute $J_{\sigma^{k+1}}(\tilde{\mathbf{x}}_{k+1})$ using Algorithm 1
  **end for**
  Determine $\sigma^{k+1,rollout}$ according to (4.4)
  Choose $\sigma_{k+1}$ as the first entry of $\sigma^{k+1,rollout}$
  Wait until $t = t_{k+1}$
  Execute mixing action $\sigma_{k+1}$
**end for**

Note that $\Xi_\sigma(k_2, k_1) = I$ if $k_2 = k_1$. Using (4.7) and (3.12), the cost function (3.18) can be written as a quadratic cost function

$$J_{\sigma^k}(\mathbf{e}) = \mathbf{e}^\top P_{\sigma^k}\mathbf{e}, \tag{4.8}$$

where $P_{\sigma^k}$ is given by

$$P_{\sigma^k} = \sum_{l=k}^{k_F-1} \beta_l \Xi_{\sigma^k}(l,k)^\top Q \Xi_{\sigma^k}(l,k). \tag{4.9}$$

Typically, $P_{\sigma^k}$ is a full matrix of size $N \times N$. Additionally as mentioned, the mapping method is only accurate if $N$ is sufficiently large. For these reasons, it is in most cases impractical to compute and process $P_{\sigma^k}$ due to memory limitations. Hence, the cost function $J_{\sigma^k}(\mathbf{e})$ has to be computed via an on-line method. On-line computation can be realized via a step-by-step approach as shown in Algorithm 1 which does not require to store full matrices of size $N \times N$. Given this fact, the closed-loop rollout policy given by (4.4) can only be realized via online computation of $J_{\sigma^k}(\mathbf{e})$. Fortunately, due to the sparsity of $\Phi_{\sigma_k}$, the computational requirements remain tractable.

To overcome the required time for solving (4.4), which would yield delays in the mixing process, we determine the control input one step in advance. The control algorithm is applied to the predicted state $\tilde{\mathbf{e}}_{k+1}$ instead of the currently measured state $\mathbf{e}_k$, where $\tilde{\mathbf{e}}_{k+1} = \Phi_{\sigma_k}\mathbf{e}_k$. This allows us to compute $\sigma_{k+1}$ in between $t_k$ and $t_{k+1}$ as shown in Algorithm 2 where we start with a pre-defined initial action $\sigma_0$. Hence, as long as the time to solve (4.4) is less than $\Delta t$ at each time-step, no additional delays occur in the mixing process.

# 5 Simulation and experiments

In the following section, the method is validated via both numerical simulations and real experiments on the well-known journal bearing flow. First, we discuss the journal bearing setup, after which we present the corresponding simulation and experimental results whereby we will aim to achieve the best mixing performance, measured by intensity of segregation at a certain terminal time $t_{k_F}$.

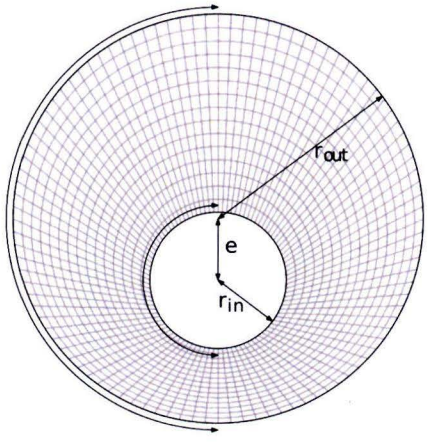


Figure 5.1: Journal bearing geometry determined by two dimensionless parameters $r = \frac{r_{in}}{r_{out}}$ and $\epsilon = \frac{e}{r_{out}}$. The gray lines represents the journal bearing grid which discretizes the domain in radial and tangential direction. In the simulations, a finer grid is used of 600x100.

## 5.1 Description journal bearing setup

The journal bearing system exists of two long eccentric cylinders, which is a benchmark system in the area of mixing, since it is a well-known, realizable, prototype 2-D flow in which chaotic mixing can appear [50]. Furthermore, an analytic expression for the velocity field is available [54] which solely depends on the geometry of the setup, making accurate simulations possible. The geometry of the setup is set by two dimensionless parameters being the ratio of the radii of the two cylinders, $r = r_{in}/r_{out}$ and the eccentricity, $\epsilon = e/r_{out}$ where $e$ is the distance between the centers of the two cylinders (shown in Figure 5.1). In this study, the parameter values are $r = 1/3$ and $e = 3/10$.

Mixing is achieved by alternating rotational movements of both cylinders. For the sake of simplicity, we only consider mixing actions for which only one of the two cylinders turns at any particular instant of time. In that case, only the displacement of the cylinders affect the results and not the chosen velocity profile. This is not true when both cylinders turn simultaneously. Moreover, mixing protocols whereby both cylinders can turn simultaneously lead to similar qualitative results [50]. In this study we restrict ourselves to four mixing actions ($M = 4, m \in \mathcal{M} = \{1, 2, 3, 4\}$); rotation of the inner and outer cylinder over fixed angles, both in counter and clockwise direction. The chosen velocity profiles are constant and the rotational angles are such that all mixing actions induce the same amount of kinetic energy per time instant into the fluid leading to angles of rotation $\theta_{in} = (1/r)\theta_{out}$ and angular velocities $V_{in} = (1/r)V_{out}$, where the inner angle of rotation is chosen as $\theta_{in} = 3\pi$. In this way, a fair comparison among mixing actions can be made. A mapping matrix is calculated for each mixing action as explained in Section 3.1. The grid used is shown in Figure 5.1.

The experimental realization of the journal bearing setup, shown in Figure 5.2, should meet two requirements. First, the setup should be able to rotate both cylinders independently where it is favorable to be able to adjust the velocity wave form which is realized via two separate servomotors. Secondly, it must be possible to be observe the entire mixing domain without any obstructions. For this reason, the bin which will be filled with polymer, has a transparent bottom and the setup is constructed such that the bottom view is clear as shown in Figure 5.2. Furthermore, during the experiments, a plain white background is placed on top of the bin around the inner cylinder. In this way, no camera calibration is required since a homogeneous offset to the state does not influence the intensity of segregation. Using a PC running a Matlab/Simulink environment and a real-time data-acquisition device based on EtherCAT, the motors are driven and camera frames are captured simultaneously in real-time.

As mentioned before, a flow is in Stokes regime if the dimensionless Reynolds number $Re = V_{mean}L/\nu$ is small, i.e. $Re << 1$. In order to achieve such a flow, a Newtonian viscous fluid is

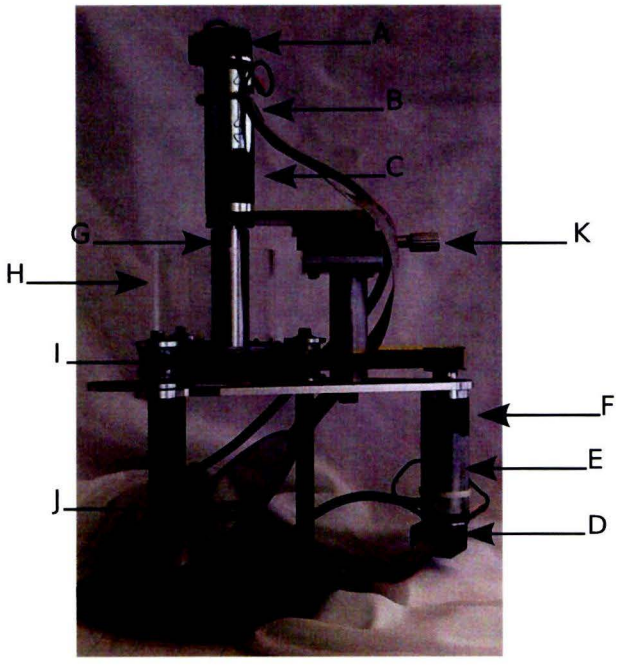


Figure 5.2: Experimental setup with A: encoder of the inner cylinder, B: (servo)motor of the inner cylinder, C: gear of the inner cylinder, D: encoder of the outer cylinder, E: (servo)motor of the outer cylinder, F: gear of the outer cylinder, G: inner cylinder, H: outer cylinder, I: transmission belt, J: mirror, K: mechanism to adjust the eccentricity.

used for the experiments, namely polydimethylsiloxane hydroxy terminated (PDMS) which has a static viscosity in the range of $\nu \approx 1.8 \cdot 10^{-3} - 2.2 \cdot 10^{-3}[\mathrm{m}^2/\mathrm{s}]$ and a density of $\rho = 0.94 \cdot 10^3[\mathrm{kg}/\mathrm{m}^3]$. Furthermore, a relatively low velocity is chosen, $V_{out} = \pi/20[\mathrm{rad}/\mathrm{s}]$. Based on the velocity profile of the narrowest section of the journal bearing setup, this yields an average velocity of $V_{mean} = 0.0042[\mathrm{m}/\mathrm{s}]$. The typical length is chosen to be the diameter of the journal bearing, i.e. $L = 2r = 75 \cdot 10^{-3}[\mathrm{m}]$. This results in a Reynolds number of $Re \approx 0.0176$. In order to exclude bottom effects such that the flow can be regarded as 2-D, the contrast fluid is dropped at the surface of a $2 \cdot 10^{-2}\mathrm{m}$ thick transparent layer of PDMS. The images of the mixture are captured with a regular USB camera underneath the setup. *See Section F of the Appendices for an extensive description of hardware and software of the set-up and Section G for an explanation on the image processing.* The velocity $V_{out} = \pi/20[\mathrm{rad}/\mathrm{s}]$ implies that in our situation, a mixing action (as $\theta_{out} = \pi$) takes $\Delta t = 20[\mathrm{s}]$. The control horizon has been set to $k_F = 30$. *See Section D of the Appendices for the motivation of this control horizon.* Hence, one experiment takes ten minutes. For this time frame, the effect of gravity is negligible.

## 5.2 Simulation results

In order to examine the performance of the rollout algorithm, we compare the rollout policy (4.4) with a periodic protocol, which is used as base policy, and the minimum error first policy (4.1). As mentioned, the chosen periodic base policy does not necessarily have to be optimal as long as the overall performance is good. Moreover, an optimal periodic protocol is difficult to determine, because the performance is highly sensitive to the initial condition which will become clear later. Therefore, the periodic base policy is determined by evaluating the overall performance by means of simulations of all possible periodic protocols of length three and four based on several initial conditions. This leads to the base policy with

$$\sigma_0^{\text{base}} = v_0 = 3, \sigma_1^{\text{base}} = v_1 = 3, \sigma_2^{\text{base}} = v_2 = 1, \sigma_3^{\text{base}} = v_3 = 1, \tag{5.1}$$

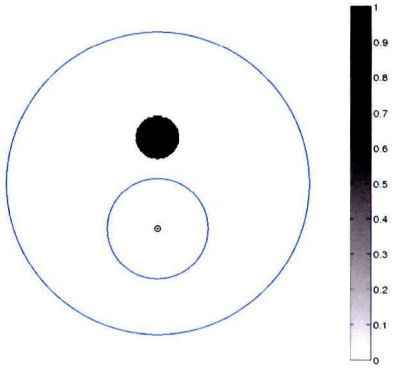


Figure 5.3: Initial concentration field used for the simulations.

which is repeated according to

$$\sigma_{k+K}^{\text{periodic}} = \sigma_k^{\text{periodic}} \text{ for all } k \in \{0, 1, \ldots, k_F - K\} \text{ and } K = 4, \tag{5.2}$$

*i.e.* a rotation of $2\pi$[rad] of the outer cylinder followed by a rotation of $6\pi$[rad] of the inner cylinder. Since simulations do not have time restrictions, pruning via (4.6) is omitted. Moreover, as already mentioned, if $k_{\min}$ and $n_{\min}$ are chosen sufficiently large the same results would be obtained. Since in this section we aim to achieve the best mixing performance, measured by intensity of segregation at a certain terminal time $t_{k_F}$, the tuning parameter values for $\beta_l$, $l \in \mathbb{N}$ and $\beta_{\min,l}$, $l \in \mathbb{N}$ are chosen as

$$\beta_l = \begin{cases} 1 & \text{if } l = k_F \\ 0 & \text{otherwise} \end{cases} \tag{5.3}$$

$$\beta_{\min,l} = \begin{cases} 1 & \text{if } l = k_{\min} \\ 0 & \text{otherwise.} \end{cases} \tag{5.4}$$

The initial concentration field represents a circular blob as shown in Figure 5.3. The simulation results are shown in Figure 5.4. As expected by Theorem 1, the proposed rollout policy indeed outperforms the periodic base policy (or at least does not perform worse). The MEF policy on the other hand performs worse than the periodic protocol. Although several papers [12, 34, 29] showed satisfactory results using the MEF policy, the results indicate that for this specific mixing setup the minimum error policy is not suitable due to its short control horizon.

To investigate the sensitivity to small spatial perturbations to the initial condition, we consider 25 different initial conditions each consisting of the same circular blob as shown in Figure 5.3 but slightly shifted over a small part of the mixing domain. In order to examine the effect of feedback, an open-loop rollout policy will be evaluated as well. This policy is a mixing protocol determined *a priori* using the rollout algorithm on the basis of the unperturbed initial concentration field, hence the open-loop rollout policy applies the same mixing sequence to each initial condition. In contrast, the closed-loop rollout policy results in a different sequence for each initial condition. Figure 5.5 presents the intensity of segregation after $k_F = 30$ steps $I_d(\mathbf{e}_{k_F})$ as in (3.11) for these initial conditions using the periodic protocol described by (5.1), the open-loop rollout policy and the closed-loop rollout policy. Note that for the periodic protocol, a small change can have a relatively large influence on the mixing quality. The closed-loop rollout policy reduces this deviation and shows for all initial conditions an improvement in performance. Initial conditions number 21 to 25 in Figure 5.5 in particular show that the closed-loop rollout policy is able to react to the initial condition due to the presence of feedback. It is important to notice that even though the only performance guarantee is that the closed loop rollout policy is never performing worse than the periodic protocol according to Theorem 1, even the open-loop rollout still performs significantly better compared to the periodic protocol in most cases.

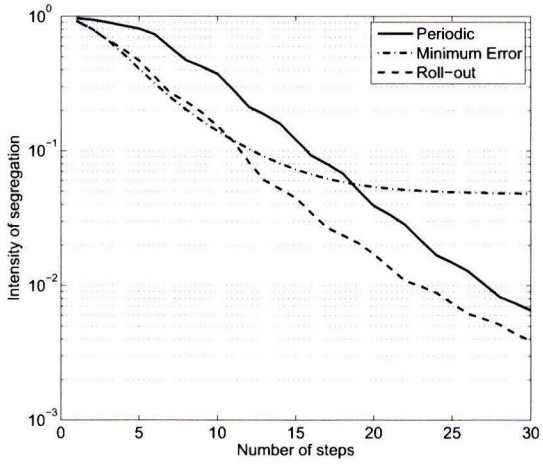


Figure 5.4: Comparison among the periodic protocol, minimum error policy and the rollout policy.

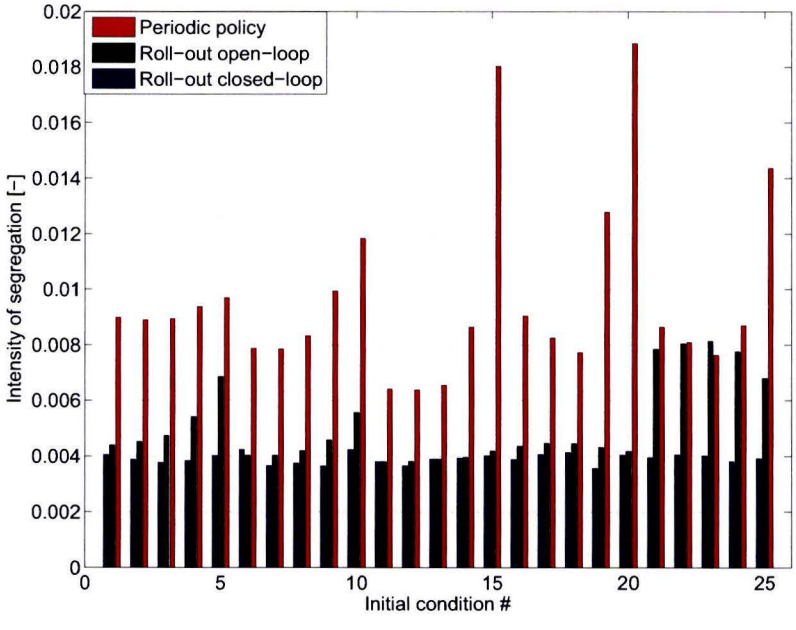


Figure 5.5: Comparison among a periodic policy, a open-loop rollout policy and a closed-loop rollout policy in terms of intensity of segregation after 30 steps, *i.e.* $I_d(k_F)$, on the basis of 25 different initial conditions whereby the chosen periodic base policy is given by (5.1) and (5.2). Note that for each initial condition, the rollout protocol indeed outperforms its base policy. Moreover, the closed-loop rollout policy reduces the variation of $I_d(k_F)$ over all 25 initial conditions.

As mentioned, the chosen periodic base policy does not necessarily have to be optimal. In fact, even a far from optimal base policy will still lead to satisfactory results. To validate this statement, we repeat the simulations presented in Figure 5.5 where we instead use the following base policy, whose performance is worse than the policy given by (5.1) and (5.2) the sequence

$$\sigma_0^{\text{base}} = v_0 = 3, \sigma_1^{\text{base}} = v_1 = 1, \tag{5.5}$$

which is repeated according to

$$\sigma_{k+K}^{\text{periodic}} = \sigma_k^{\text{periodic}} \text{ for all } k \in \{0, 1, \ldots, k_F - K\} \text{ and } K = 2, \tag{5.6}$$

*i.e.* a rotation of $\pi$[rad] of the outer cylinder followed by a rotation of $3\pi$[rad] of the inner cylinder. This base policy is used for both the open-loop rollout policy as the closed-loop rollout policy. The results of the periodic protocol described (5.5) and (5.6), the open-loop rollout policy and the closed-loop rollout policy are presented in Figure 5.6. By comparing Figure 5.5 and Figure 5.6, we can conclude that even though the performance of the periodic base policy, given by (5.5) and (5.6), is significantly worse than the performance of the periodic base policy, given by (5.1) and (5.2), the rollout policy still leads to satisfying results.

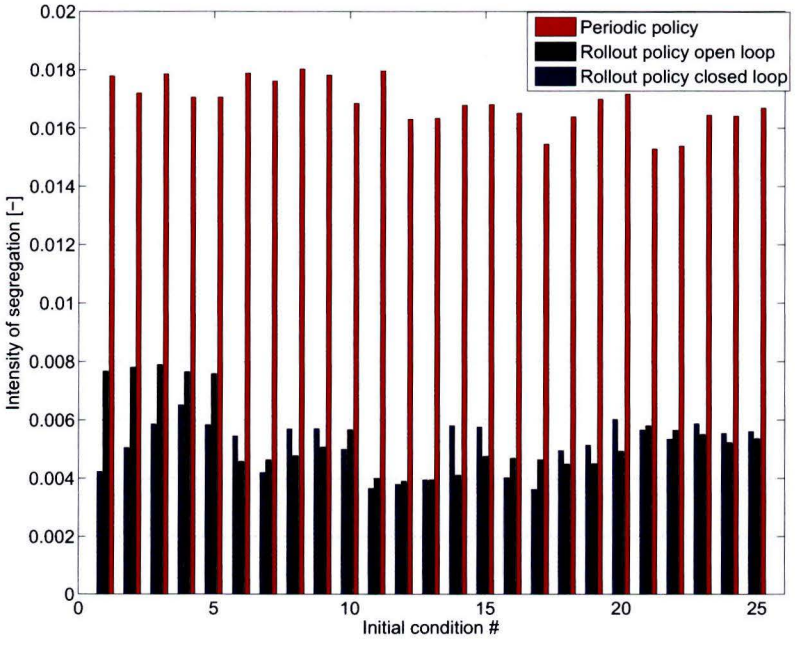


Figure 5.6: Comparison between an periodic policy, an open-loop rollout policy and a closed-loop rollout policy in terms of intensity of segregation after 30 steps, *i.e.* $I_d(k_F)$, on the basis of 25 different initial conditions whereby the chosen periodic base policy is given by (5.5) and (5.6). Note that for each initial condition the rollout protocol outperforms its base policy and even performs relatively well with respect to the periodic policy used in Figure 5.5.

## 5.3 Experimental results

The results presented in Section 5.2 already show that more effective mixing can be achieved by the feedback policy proposed in this paper. In this section, the practical feasibility and effectiveness of the proposed method will be validated. Here, measurement noise, model errors and time constraints are present. Since the control method in presented in this paper is model-based, first the mapping method is validated by means of an experiment. Figure 5.7 compares the measured state and simulated state after executing 22 steps of the periodic protocol. Clearly, the shape of the dye and thereby the spatial structure of the state coincide well. This suggests that the mapping method is indeed an accurate method for modeling the system. However, the measured concentration is more diffuse than the simulated state, which hints that diffusion plays a role in the experiment.

Next, we evaluate a closed-loop rollout policy whose base policy is described by (5.1) and (5.2) and whose tuning parameters are chosen as (5.3) and (5.4). Figure 5.8 and Figure 5.9 present the

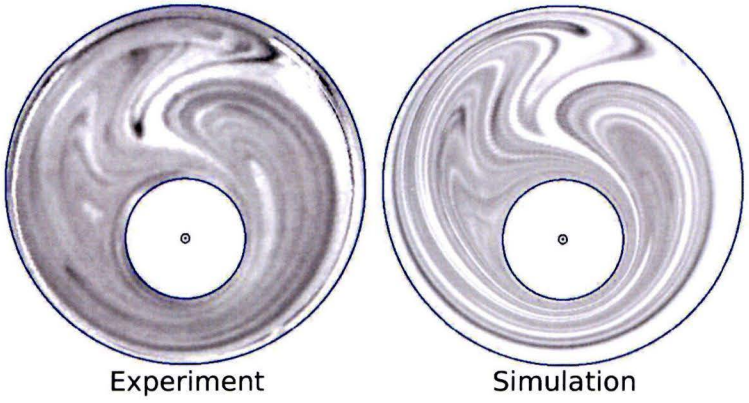


Figure 5.7: The left figure shows the measured states (in this case concentration field) after executing 22 steps of the periodic protocol. The right figure shows the simulated state after 22 steps of the periodic protocol which coincides well with the measured state. However, the measured concentration is more diffuse than the simulated state, which hints that diffusion plays a role in the experiment.

experimental results of the periodic protocol and rollout policy, respectively. Observe that in spite of the fact that the mixing process in presence of diffusion is irreversible, the intensity of segregation is not always monotonically decreasing. Moreover, Figure 5.8 and Figure 5.9 show that, although experiments are executed under the same conditions, the difference among experiments in terms of intensity of segregation is significant. Despite that for the periodic experiments shown in Figure 5.8, spatial structures of the states coincide well to each other. These observations can explained due to errors in the measurement system, *e.g.* camera noise and differences in illumination and contrast. Because of this, relating concentration to a pixel value is a difficult practical problem. Furthermore, not only errors in the measurement system are responsible for the difference between experiments, but also the inevitable small variances in initial condition.

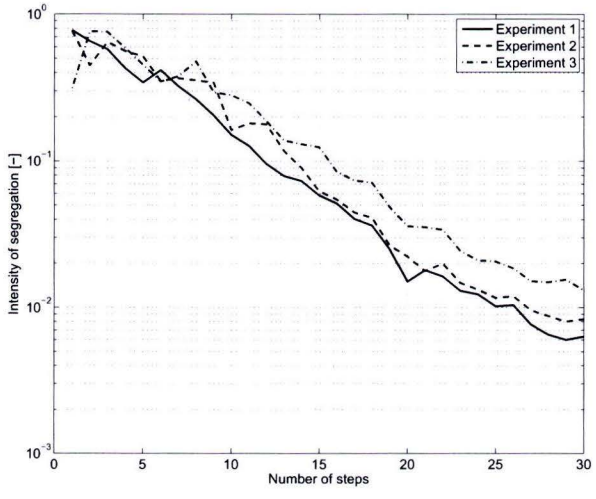


Figure 5.8: Experimental results of the periodic protocol showing the evolution of the (measured) intensity of segregation $I_d$ over time. All three experiments were executed under the approximately same conditions with the same periodic protocol. The chosen periodic protocol is given by (5.1) and (5.2), *i.e.* one whole rotation of the outer cylinder followed by three rotations of the inner cylinder. Important notice is the difference among the three experiments due to measurement uncertainties and slight variance in initial condition. Furthermore for the same reasons, the intensity of segregation is not monotonically decreasing. The average intensity of segregation over all experiments at terminal step $k_F$ is 0.0093.

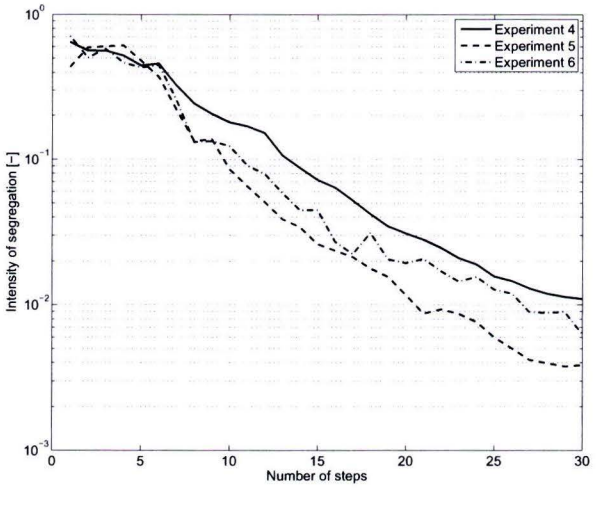


Figure 5.9: Experimental results of the closed-loop rollout policy in terms of the evolution of the (measured) intensity of segregation $I_d$ whereby the chosen periodic base policy is given by (5.1) and (5.2). All three experiments were executed under approximately the same conditions with the same periodic base policy. Important notice is the difference among the three experiments due to measurement uncertainties and slight variance in initial condition. The average intensity of segregation over all experiments at terminal step $k_F$ is 0.0070.

Figure 5.10 shows a comparison between the periodic protocol and rollout policy, on the basis of the

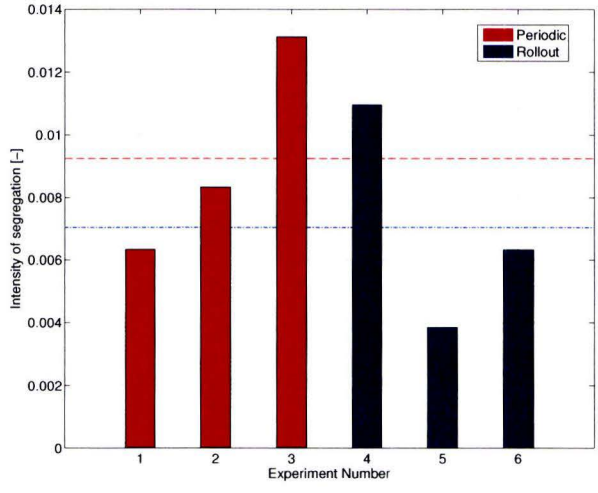


Figure 5.10: Comparison among all six experiments (three which executed a periodic protocol and three which executed a closed-loop rollout policy under the same conditions and approximately the same initial condition) in terms of (measured) intensity of segregation after 30 steps, *i.e.* $I_d(k_F)$. The red dotted and the blue dash-dotted line present the average results of the periodic protocol and the rollout policy respectively. Important to notice is that the rollout policy does not consistently outperform the periodic protocol due to the differences among experiments caused by measurement uncertainties and slight variance in initial condition. However on average, the rollout experiments yield a better intensity of segregation.

simulation results from Figure 5.8 and Figure 5.9, with respect to the final intensity of segregation. Due to measurement errors as discussed before, the rollout policy does not always outperform the periodic protocol in terms of (measured) intensity of segregation. However on average, the rollout experiments yield a lower intensity of segregation.

To overcome these measurement errors, the experimental mixing protocols are evaluated by means of post-experimental simulations based on the measured initial states. The results are presented in Figure 5.11. In all cases, the rollout policy outperforms the periodic protocol. This observation shows that in spite of the measurement uncertainties, the feedback controller is still able to construct a well-performing mixing protocol. This can be explained by the fact that the entire state is used in the feedback controller. As shown by Figure 5.7, the global spatial structure of this state corresponds well to the corresponding model prediction. Note that a comparison between Figure 5.10 and Figure 5.10 shows that even though the mapping method is an accurate method for modeling the system as suggested by Figure 5.7, the intensity of segregation of the post-experimental does not coincide with the intensity of segregation measured in the experiments. For this reason, we consider an experiment whereby the contrast of the camera images has been adjusted such that the measured intensity of segregation matches the predicted intensity of segregation. In addition, the periodic protocol given by (5.5) and (5.6) is chosen as base policy whose performance is considerably worse than the periodic protocol used in previous experiments. In that case, we can expect a more obvious gain in performance in spite of measurement errors since, as discussed in Section 5.2, even a far from optimal base policy will still lead to satisfactory results. Figure 5.12 provides a comparison between the periodic protocol described by (5.5) and (5.6) and the closed-loop rollout policy using this same periodic protocol as base policy by means of a plot which shows the evolution of both the measured and post-experimental simulated intensity of segregation. Now, we can clearly see in both experiments and post-experimental simulations that the rollout policy outperforms its base policy. In fact, the closed-loop rollout policy has already reached the final intensity of segregation of the periodic protocol after 20 steps.

The results presented in this section show that the proposed method is indeed feasible and effec-

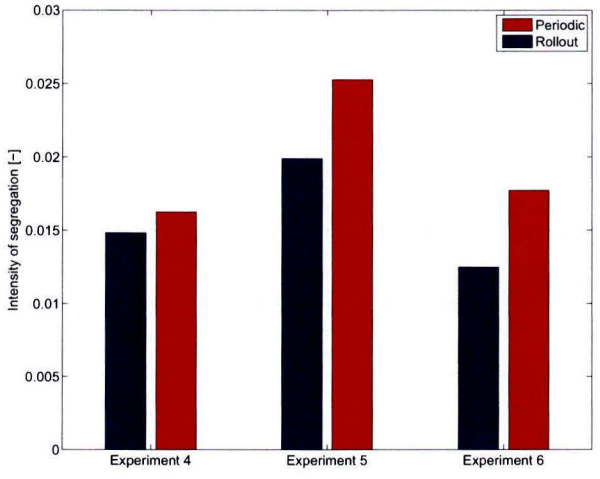


Figure 5.11: Post-experimental simulation results on the basis of the measured initial states and mixing protocols constructed during the experiments. The blue bars correspond to a simulation of the periodic protocol applied on the measured initial condition of the corresponding experiment and show the resulting intensity of segregation after 30 steps, *i.e.* $I_d(k_F)$. The red bars correspond to a simulation of the protocol constructed by the closed-loop rollout policy during the corresponding experiment and show resulting $I_d(k_F)$. In all three cases, the rollout policy outperforms the periodic protocol.

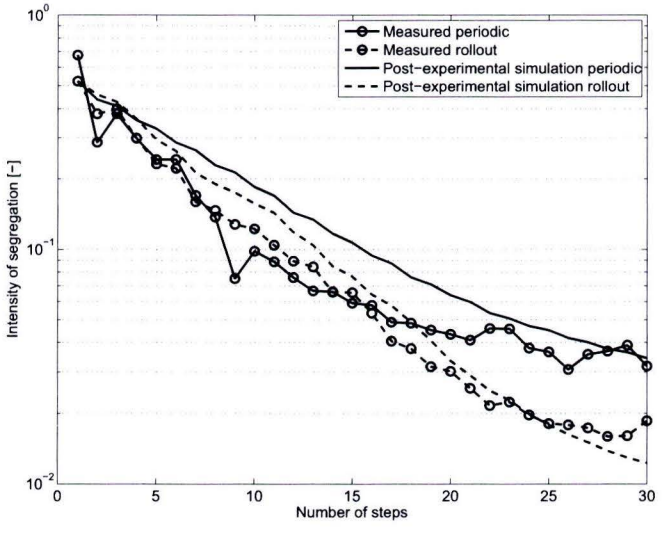


Figure 5.12: Experimental results in terms of the evolution of the (measured) intensity of segregation $I_d$ of two experiments; one which executed a closed-loop rollout policy and one which executed the periodic base policy whereby the chosen periodic base policy is given by (5.5) and (5.6). Despite the base policy is far from optimal, the closed-loop rollout policy leads to improved mixing and clearly outperforms its periodic base policy. In fact, the closed-loop rollout policy only requires 20 steps to obtain the same level of intensity of segregation as the periodic protocol after 30 steps. Note that the simulations and experiments are closer too each other than in previous experiments. However, still a difference is visible due to measurement errors.

tive in practical context. In spite of the measurement uncertainties, post-experimental simulations revealed that the closed-loop rollout policy still managed to construct well-performing mixing protocols. Furthermore, the performance guarantee of the rollout policy described in Theorem 1 was clearly observed in Figure 5.12. These observations provide a clear proof-of-concept.

*An analysis of the experiment errors is given in Section H of the Appendices*

# 6 Conclusions

In this paper we studied optimal fluid mixing from a switched system perspective. This perspective allowed us to obtain a systematic methodology for designing feedback laws resulting in well-performing aperiodic mixing protocols. In order to obtain a practically feasible problem setup, three main steps were taken. At first, the domain was discretized into a finite number of cells. Secondly, the mixing process was sampled at discrete time instants. Thirdly, we considered a finite set of control inputs/mixing actions. By exploiting the cell mapping method [31], the resulting system could be modeled as a *switched system*, and the mixing protocol is given by a sequence of scheduling variables, each one corresponding to a mixing action. These ingredients were used to formulate an optimal control problem that allows different objectives and definitions of mixing efficiency. In this way, we could use rollout algorithms [8] which guarantee that the resulting feedback policy outperforms any available periodic mixing sequence, which is an important performance guarantee.

Both simulation and experimental results provided clear evidence of the benefits of the proposed framework for the design of aperiodic (open-loop or feedback) policies for effective mixing of fluids. Simulations of the periodic protocols, minimum error first policies and our rollout policies revealed that minimum error first policies do not always lead to satisfactory results which motivates the use of rollout policies. Furthermore, our method appears to be useful not only for designing closed-loop solutions, but also for creating open-loop protocols as well. In addition, it was clear that feedback solutions make the system less sensitive to perturbations in initial conditions and modeling errors. Finally, we observed that even a far from optimal base policy will still lead to satisfactory results and thus constructing a suitable base policy does not require extensive optimizations. All these observations provide a clear proof-of-concept for the proposed ideas. Indeed, the results show significant improvement in mixing with respect to existing solutions and real-time feasibility of the setup.

Obtaining consistent experimental results regarding to measured intensity of segregation however appeared to be a hard problem, since relating concentration to a pixel value is non-trivial. Directions for future work could be to develop a more accurate measurement system, to verify the proposed methodology to other benchmark, *e.g.* time-periodic sine flow [11, 12, 25, 36], lid-driven cavity flow [31] and the blinking vortex flow [55] , to quantify the sensitivity to modeling errors, *e.g.* the mismatch in diffusivity, and the presence of measurement errors and to apply the proposed method to industrially relevant mixers.

# Part III
# Additional conclusions

In Section 6, we came to the conclusion the framework proposed in Part II is a suitable methodology for the design of aperiodic (open-loop or feedback) policies to achieve effective mixing. Important observations were that minimum error policies do not always lead to satisfactory results, that feedback makes the systems less sensitive to perturbations in initial condition and modeling errors and that even a far from optimal base policy will still lead to satisfactory results.

As mentioned, directions for future work could be to quantify the sensitivity to modeling errors and the presence of measurement errors. Based on the work presented in Appendix C and Appendix E we can already come to some conclusions in these directions. Appendix C.1 evaluates the controller from a physical point of view via an eigenmode analysis of the mapping matrices. These eigenmodes represent typical spatial structures which occur in the mixing process. Hereby the slow decaying eigenmodes, in the sense that their characteristic time scale is large, correspond to the relatively large structures in the mixtures and the fast decaying eigenmodes to the more detailed structures. In general, measurement errors like camera noise manifest itself in relative small spatial structures corresponding to fast decaying modes. Therefore, if a measured state is evaluated over a sufficiently large horizon, the influence of camera noise becomes irrelevant. Given these facts, the closed-loop system is in general not sensitive to camera noise. For this reason, as observed in section 5.3, the closed-loop rollout policy still constructs well-performing mixing protocols in spite of the presence of measurement errors. Moreover, this implies that the controller particularly reacts to relatively large spatial structures in the flow domain and therefore prevents island to occur. Appendix C.2 provides a more intuitive and visual evaluation of the closed-loop mixing process. Hereby it was shown that the rollout policy causes repetitive stretching and folding, the general mechanism for effective mixing [45].

In Appendix E, the influence of a diffusivity mismatch was examined by means of simulations. In general, a diffusivity mismatch degrades the performance of the rollout algorithm. Furthermore, the results showed that feedback has no significant role with respect to a diffusivity mismatch. Therefore, it is recommended to incorporate the molecular diffusion if present into the controller model in stead of using a model which assumes pure advection. In case computational resources are limited, it is not always possible to use an accurate model. In that case, a model with a coarser grid has to be used. However, the system is less affected in case the diffusivity of the controller model is larger than the case the model's diffusivity is smaller than the diffusivity of the plant. Moreover, using a coarser grid emphasizes the most dominant modes since the eigenvalue spectrum contracts to the origin [23, 24] which makes the system less sensitive to input noise. Important to notice is that effect of the numerical diffusion is not the same as molecular diffusion.

# Part IV
# Appendices

## A Detailed problem description

The present study concerns mixing in two-dimensional incompressible Stokes flows. Note that three dimensional flows can be approached in a similar fashion. Let $c(\mathbf{x},t) \in [0,1] \subset \mathbb{R}$ be a normalized, positive, conserved scalar quantity in a domain $\Omega \subset \mathbb{R}^2$ associated with a physical transported entity (e.g. temperature, concentration) where $\mathbf{x} = (x,y)^\top$ are Cartesian coordinates. The evolution of $c(\mathbf{x},t)$ is governed by the advection-diffusion equation derived from on the conservation property of $c(\mathbf{x},t)$:

$$\frac{\partial c}{\partial t} = -\mathbf{v}(\mathbf{x},t)\cdot\nabla c + \frac{1}{Pe}\Delta c, \tag{A.1}$$

where $\mathbf{v}(\mathbf{x},t)$ denotes the velocity field which is divergence-free because of incompressibility. Here $Pe = \frac{VL}{D}$ is the Péclet number, with $V$ the characteristic velocity scale, $L$ the characteristic length scale and $D$ the mass diffusion coefficient. Since $c(\mathbf{x},t)$ is conserved *i.e.* $\int_\Omega c(\mathbf{x},t)dA$ is constant, complete mixing in the domain $\Omega$ is achieved if $c(\mathbf{x},t) = \bar{c} = \frac{\int_\Omega c(\mathbf{x},t)dA}{\int_\Omega dA}$ for all $\mathbf{x} \in \Omega$, where $\bar{c}$ is the average of $c(\mathbf{x},t)$ over $\Omega$. See [55] for a mathematical rigorous definition of mixing related to chaos theory. In case diffusion is absent, which corresponds to the limit $Pe \to \infty$, the entity corresponding to $c(\mathbf{x},t)$ is only being transported over the domain. This implies $\int_\Omega |c(\mathbf{x},t) - \bar{c}|dA$ is constant and strictly speaking, no mixing occurs. Hence, diffusion is responsible for the homogenization of $c(\mathbf{x},t)$, *i.e.*

$$\lim_{t\to\infty}\int_\Omega |c(\mathbf{x},t) - \bar{c}|dA \to 0. \tag{A.2}$$

Hence, one aspect of enhancing mixing is to increase the effect of molecular diffusion which can be achieved by a reduction of the characteristic length scales. Therefore, the general mechanism for effective distributive mixing is repetitive stretching and folding of material elements [45], which leads to an increase of the intermaterial contact area [40] and a decrease of length scale and therefore enhances the effect of molecular diffusion.

The mechanism of repetitive stretching and folding is in general achieved by inducing chaotic behavior. The particle trajectories are determined by a set of two first order nonlinear ordinary differential equations

$$\frac{d}{dt}\mathbf{x} = \mathbf{v}(\mathbf{x},t). \tag{A.3}$$

Since the system expressed in (A.3) has three state variables, namely two spatial variables $x, y$ and one temporal $t$, it can exhibit chaotic behavior [2]. In case of a non linear differential equation with only one or two dynamical variables, the system is an integrable Hamiltonian system where integrability implies regular trajectories.

A velocity field $\mathbf{v}(\mathbf{x},t)$ corresponding to an incompressible Stokes flow should comply with

$$\frac{\partial \mathbf{v}}{\partial t} = -\nabla p + \mu\Delta\mathbf{v} + \mathbf{f}(\mathbf{x},t) \text{ in } \Omega\times(0,\infty) \tag{A.4}$$

$$\mathbf{v}(\mathbf{x},t) = \mathbf{g}(\mathbf{x},t) \text{ on } \partial\Omega\times(0,\infty) \tag{A.5}$$

where $\mathbf{g}(\mathbf{x},t)$ corresponds to the imposed boundary motions. In case of stationary boundary motions i.e. $g(\mathbf{x},t) = g(\mathbf{x})$, stationary pressure gradient i.e. $\frac{\partial}{\partial t}\nabla p = 0$ and stationary external body forces i.e. $\mathbf{f}(\mathbf{x},t) = \mathbf{f}(\mathbf{x})$, the velocity field evolves to a stationary velocity field *i.e.* $\lim_{t\to\infty}\frac{\partial \mathbf{v}(\mathbf{x},\infty)}{\partial t} = 0$. Hence, in the limit where $t$ goes to infinity no chaotic behavior occurs. Therefore, in two-dimensional systems, chaotic advection is achieved by time-varying boundary motions $g(\mathbf{x},t)$, pressure gradients $\nabla p(\mathbf{x},t)$ and/or body forces $\mathbf{f}(\mathbf{x},t)$ which are established in the mixing protocol whereby a mixing action at time $t$ is defined as the tuple $(\mathbf{g}(\mathbf{x},t), \nabla p(\mathbf{x},t), \mathbf{f}(\mathbf{x},t))$. Important to notice is that chaotic advection

can occur in three dimensional flows even if they are stationary. The mixing behavior of such flows are determined by the geometry of the system. Mixing devices designed according to this principle are known as static mixers. In this paper, we focus on two-dimensional flows. Hence, assuming a fixed amount of time is available for mixing, the ideal goal is to find an optimal policy which maps the current (measured) scalar field $c(\mathbf{x}, t)$ to an optimal mixing action $(\mathbf{g}(\mathbf{x}, t), \nabla p(\mathbf{x}, t), \mathbf{f}(\mathbf{x}, t))$.

**Remark** Although one can find the term 'chaos' defined in textbooks, there is no universal acceptance of a single definition. However, in this work we refer a map on an invariant set to be chaotic if it is ergodic and the orbits have some positive Lyapunov exponent (growth rate of infinitesimal perturbations) [55].

Obtaining a mathematical formulation of this infinite-dimensional problem might be tedious. In addition, even if such a formulation would be obtained, it would be intractable due to the infinite-dimensional character of the problem. For this reason, the conventional methodology to solve this control problem is analyzing mixing as a function of the period of a time-periodic flows. Hence, they focus on defining methodologies for constructing advection cycles of period $T$ defined by $(\mathbf{g}(\mathbf{x}, t), \nabla p(\mathbf{x}, t), \mathbf{f}(\mathbf{x}, t))$ where $(\mathbf{g}(\mathbf{x}, t+T), \nabla p(\mathbf{x}, t+T), \mathbf{f}(\mathbf{x}, t+T)) = (\mathbf{g}(\mathbf{x}, t), \nabla p(\mathbf{x}, t), \mathbf{f}(\mathbf{x}, t))$ for all $t \in \mathbb{R}^+$. Typically, these type of flows contain periodic points. Consider the following first order non-linear differential equation:

$$\dot{\mathbf{x}} = f(\mathbf{x}, t), \tag{A.6}$$

where $f$ is sufficiently smooth. Let $\Phi_T$ be a continuous transformation according to (A.6), corresponding to an advection cycle over a time frame $T$ such that

$$\mathbf{x}(t+T) = \Phi_T(\mathbf{x}(t)), \tag{A.7}$$

then a point $\mathbf{p} = \begin{pmatrix} x \\ y \end{pmatrix}$ is called periodic of period $T$ if

$$\mathbf{p} = \Phi_T(\mathbf{p}). \tag{A.8}$$

In homogeneous incompressible flows (*i.e.* divergence free velocity field) , the stability type of periodic points are either elliptic or hyperbolic. The stability type can be determined by calculating the eigenvalues of the Jacobian. If the eigenvalues are equal to zero the periodic point is elliptic, else it is hyperbolic. Since the map is area preserving, the stability can also be determined from the trace of the Jacobian matrix. A trace less then two correspond means that the point is elliptic, a trace greater than two means the point is hyperbolic. In flows elliptic periodic points are typically centers of islands, i.e. regular regions. In these regions, fluid particles remain on closed invariant curves, known as KAM (Kolmogorov-Arnold-Moser) tori, under the advection cycle. This implies that these trajectories are confined to a lower-dimensional subspace of the phase space and therefore form transport barriers to scalar redistribution. In other words, these KAM tori separate the islands from their surroundings. Hyperbolic points will stretch nearby fluid elements which enhances local mixing behavior. These regions are referred as chaotic seas. [40, 50]

A Poincaré section shows behavior of the fluid for several different initial conditions over discrete time steps $T$ corresponding to the length of an advection cycle. After sufficient advection cycles, this section reveals the chaotic seas (mixing) and regular (non-mixing) regions. In some literature [49], these structures are referred as Lagrangian coherent structures (LCSs). Regular regions appear as closed invariant curves, also known as (quasi)-periodic orbits or KAM tori, and chaotic seas as scattered points which means there is no apparent structure present in the flow trajectories. In some cases it is hard to distinguish these two types of behavior, a regular region is often slightly scattered because of numerical errors and a thin chaotic sea may look as a regular orbit.

In order to obtain an effective advection cycle, islands should be avoided. However, finding elliptic periodic points is not trivial and flow specific. Moreover, it is not always possible to find conditions for all periodic point being hyperbolic. Hence most industrial mixers rely on heuristics [18]. Aperiodic flows are devoid of periodic points which motivates the use of aperiodic mixing protocols as suggested by Liu [34].

# B Literature review mixing control

Liu *et al.* [34] proposed the use of aperiodic mixing protocols since aperiodic flows are devoid of periodic points. To the authors' knowledge, Aamo *et al.* [1] were the first to induce mixing by means of feedback control. The paper aims to enhance mixing in a 2D channel flow induced by perturbations at the boundary. At first, they deduce a decentralized control law in order to stabilize the parabolic velocity profile. Secondly, this controller is reversed (by changing the sign) in order to destabilize the flow leading to unsteadiness in the flow. Their conjecture is that a unstable flow will develop a complicated pattern in which mixing will occur. The approach was verified by means of simulations using dye surface length and probability of well mixedness as mixing measure. Note that this approach only uses feedback for destabilizing the flow and does not directly control the mixing behavior

D'Alessandro *et al.* [15] approaches the mixing problem from a kinematical point of view, namely by defining the maximum entropy as mixing measure. Entropy in the context of dynamical systems theory was introduced as a measure of disorder created by a transformation. Pesin's formula *et al.* [44] shows that entropy is equal to the stretching rate (given by the Lyapunov exponents) averaged over the whole phase space. Hence, mixing can be enhanced by finding sequence of flows which maximizes the entropy of the system. In the paper, tools from ergodic theory are for the formulation and solution of this control problem.

Hoeijmakers *et al.* [27] bridges the gap between the purely statistical and the purely kinematical descriptions of mixing by adopting the hydrodynamic entropy. The paper focuses on optimizing the flow for an array of vortices by means of input-output linearization. Furthermore, they investigate the relation between mixing and stationary viscous dissipation. The main conclusion is that statistical properties of the hydrodynamical entropy may indeed contribute to a better understanding of mixing. The works mentioned above does not take the initial orientation of the scalar field into account in contradiction to Mathew *et al.* [36], Cortelezzi *et al.* [12] and Couchman *et al.* [13].

Mathew *et al.* [36] introduced a new formalism for optimal control of advective mixing in aperiodic flows by combining a multiscale mixing measure [37] and concepts form finite-horizon optimal control theory. They consider the optimization of velocity fields constructed by superposition of practical realizable velocity fields:

$$\mathbf{v}(\mathbf{x},t) = \sum_{i=1}^{n} \alpha_i(t)\mathbf{v}_i(\mathbf{x}). \tag{B.1}$$

The paper's focus is to find $\alpha_i(t)$ such that best mixedness is achieved at time instant $t_f$. It uses the conjugate gradient method in order to find a suboptimal solution to this problem. Note that such an approach can only guarantee convergence to local minima. Moreover, the paper does not concern feasibility and efficiency in practical contexts.

Cortelezzi [12] investigates the feasibility, efficiency and transportability of short-time-horizon optimal mixing protocols. They consider a blinking velocity field, the flow is governed by instantaneously switching velocity fields acting over a time $\tau$. In terms of (B.1), $\alpha_i(t)$ can either be '0' or '1'. Hence, the protocol to be optimized can be regarded as the string $\{\alpha_1, \alpha_2, \ldots, \alpha_N\}$. Given a switching time horizon $\nu$, the optimization is based on a minimum error approach where several sub-protocols of length $\nu$ are being evaluated and the best one is selected. This approach yields a sub-optimal solution and can both be applied in open-loop or closed loop fashion. However, they only concern a sine-flow for which an analytical solution for the position of a tracing particle exists. Furthermore, no performance guarantees are derived.

Recently, Couchman [13] proposed a novel closed loop solution to mixing problem where the velocity field consists of a steady base flow and a modulated flow, *i.e.* a flow given by (B.1) where $\alpha_1(t) = 1$, $\alpha_2(t)$ is the control input and $\alpha_i(t) = 0$ for $i \in \{3, \ldots, n\}$. By using Fourier differentiation matrices and spatial discretization of the state, the problem can be formulated as a bilinear quadratic regulator problem (BQR). The problem is modified by adding a non-negative state-penalizing term (aBQR) such that the closed-form solution can be approached. This yields a simple control law. The main advantage is that the closed-loop system will inherently reject disturbances but there are no theoretical performance guarantees. At last, one interesting conclusion was made; a well-performing controller can be designed around a model with significantly larger diffusivity than that of the plant.

# C Physical interpretation controller

## C.1 Modal analysis

Based on (A.1), periodic scalar transport can be described by the Floquet operator $\mathcal{F}$ which maps the scalar distribution between discrete times levels $t = nT$, where $n \in \mathbb{N}$ and $T$ is the time of one period, via

$$c(\mathbf{x}, (n+1)T) = \mathcal{F}(c(\mathbf{x}, nT)) \tag{C.1}$$
$$c(\mathbf{x}, nT) = \mathcal{F}^n(c(\mathbf{x}, 0)) \tag{C.2}$$

The Floquet operator (equation C.1 and C.2) admits the eigenmode decomposition

$$c(\mathbf{x}, nT) = \sum_{k=0}^{\infty} \gamma_k \mathcal{H}_k^{(n)}(\mathbf{x}), \quad \mathcal{H}_k^{(n)}(\mathbf{x}) = v_k^n \Theta_k(\mathbf{x}) \tag{C.3}$$

with $\mathcal{H}_k^{(n)}$ the eigenmodes and $\{\Theta_k, v_k\}$ the corresponding eigenfunction-eigenvalue pairs governed by the eigenvalue problem $\mathcal{F}(\Theta_k) - v_k\Theta_k = 0$. The spectral structure of the Floquet operator correspond to LCSs.

The mapping matrices $\mathbf{\Phi}$ and $\mathbf{\Xi}$ are discrete approximations of the Floquet operator $\mathcal{F}$ (C.1), (C.2), therefore their eigenvector-eigenvalue pairs are discrete counterparts to the eigenfunction-eigenvalue pairs $\{\Theta_k, v_k\}$ of $\mathcal{F}$ (C.3). Hence,

$$c(\mathbf{x}, nT) = \mathbf{\Phi}^n c(\mathbf{x}, 0) = \sum_{k=1}^{N} \tilde{c}_k^0 \mathbf{h}_k^{(n)}, \quad \mathbf{h}_k^{(n)} = \lambda_k^n \mathbf{v}_k, \quad c(\mathbf{x}, 0) = \sum_{k=1}^{N} \tilde{c}_k^0 \mathbf{v}_k, \tag{C.4}$$

where $\mathbf{v}_k$ and $\lambda_k$ satisfy the equation

$$\Phi \mathbf{v}_k = \lambda_k \mathbf{v}_k. \tag{C.5}$$

The eigenmodes modes of the mapping matrices reveal the LCSs, i.e. islands and chaotic seas. The correlation between eigenmodes and LCSs is revealed by the study by Singh *et al.* [48] and Speetjens *et al.* [49]. The key findings have been condensed in the following properties:

**Property 1** *Elliptic islands relate to eigenmodes with* $|\lambda_k| = 1$

**Property 2** *Chaotic seas have eigenmodes with* $|\lambda_k| < 1$

**Property 3** *Eigenmodes of elliptic islands and chaotic seas are spatially disconnected. To this end eigenmodes must not affect the spatiotemporal scalar evolution outside their associated spatial entities.*

**Property 4** *Period-p structures of equal kind correspond with clusters of eigenvalues* $\{\lambda^{(0)}, \lambda^{(1)}, \ldots, \lambda^{(m)}, \ldots, \lambda^{(p-1)}\}$, *with* $\lambda^{(m)} = |\lambda|\omega^n$ *and* $\omega = e^{2\pi i/p}$

**Property 5** *The active zones of all eigenvectors* $\mathbf{v}_j^{(m)}$ *combined demarcate the invariant region occupied by the entire period p group in the asymptotic advection pattern.*

Note that these properties pertain specially to conformal mapping grids which means that the conjectures are only true if the grid is chosen such that there are strict separations between LCSs. For non-conformal grids, all eigenvalues except the one corresponding to the trivial eigenmode associated with global mass conservation, lie inside the unit disc. However, if the grid size is small enough, the conjectures are retained to a high degree of accuracy.

The eigenmodes belonging to eigenvalues near the unit disk, hence the slow decaying modes in the sense that their characteristic time scale is large, are the dominant eigenmodes of the system. The behavior of the mixture is mainly determined by these modes. Therefore, the spatial structure of these dominant eigenmodes are visible in the state of the system when the same mapping is applied for several times, see also (C.4). The dominant eigenmodes correspond to the relatively large structures

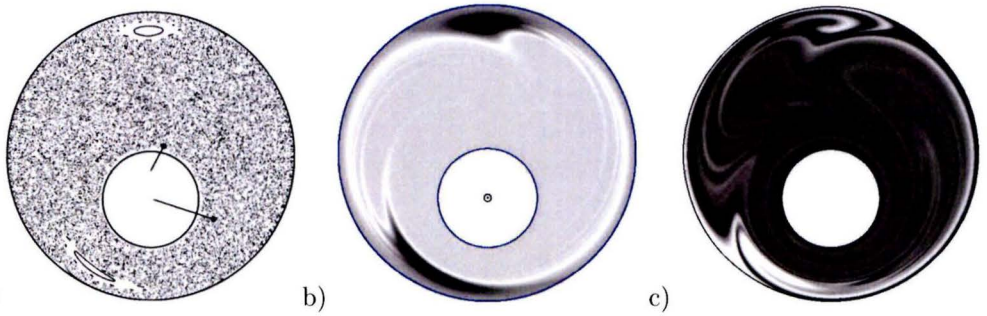


Figure C.1: Comparison between a) Poincaré section (source: [20]), b) dominant eigenmode and c) scalar field after 24 periods for a periodic flow ($\theta_{out} = 2\pi$ followed by $\theta_{in} = 6\pi$).

in the mixtures and the fast decaying eigenmodes to the more detailed structures. Measurement errors like camera noise often manifest itself in relative small spatial structures corresponding to fast decaying modes, *i.e.* their characteristic time scale is small. Therefore, these modes become irrelevant when a measured state evaluated over a sufficiently large control horizon. Given these facts, the closed-loop system is in general not sensitive to camera noise. For this reason, as observed in section 5.3, the closed-loop rollout policy still constructs well-performing mixing protocols in spite of the presence of measurement errors.

Figure C.1 illustrates the statements above using the journal bearing benchmark. The periodic protocol is chosen as the following repetitive sequence: first, the outer cylinder turns $\pi$[rad] and the inner cylinder $3\pi$[rad]. Figure C.1 a) shows the Poincaré Section created by tracing several random placed particles over a numerous of periods. The section reveals regions which are separated from the major chaotic sea. Figure C.1 a) shows the most dominant eigenmode (the mode corresponding to the second largest eigenvalue). Note this mode is not spatially disconnected from major chaotic sea due to numerical diffusion. However, the eigenvector elements corresponding to the major chaotic sea are considerably smaller. FigureC.1 b) shows the scalar field distribution after 24 advection cycles for some initial condition. The structure of the most dominant eigenmode is clearly visible.

## C.2 Velocity field versus scalar field

To gain more insight into the performance of the controller and whether its decisions can be explained, this Section provides a more intuitive and visual evaluation of the closed-loop mixing process. As mentioned in Section A, the general mechanism for effective mixing in Stokes flow domain is repetitive stretching and folding [40, 45]. Hence, a well mixing flow shows aspects of this behavior. In case of the journal bearing flow, the stretching and folding mechanism can be realized via alternation between two imposed velocity fields shown in Figure C.2(a) and Figure C.2(b). The streamlines corresponding to these fields are shown in Figure C.3. Note that both fields contain regions vortexes where the velocity components are relatively small. Hence, the stretching rate in these regions is small.

In order to verify whether the controller incorporates these facts, the controlled flow is evaluated on basis of plots whereby the concentration field is overlayed by the instantaneous vector field imposed by the boundary motions of the journal bearing. Consider the case whereby the initial condition is given by a blob. Intuitively, the stretching rate of the blob should be maximized in order to spread the blob as quick as possible over the domain. This rate is determined by the size of the velocity gradients. Figure C.2(a) and Figure C.2(b) show that by using the feedback policy introduced by Section 4, the control action is chosen such that the blob is overlapped with the largest velocity gradients. Notice that the position of the two blob coincide with the region of the vortexes (see Figure C.3).

Now we consider a more complex scalar field. Figure C.4(a) and (b) show the same concentration field which was measured during an experiment where the dye already has under come several mixing actions. Notice that Figure C.4(a) is overlapped with the vector field corresponding to a clockwise rotation of the inner cylinder and that C.4(b) is overlapped with the vector field corresponding to a

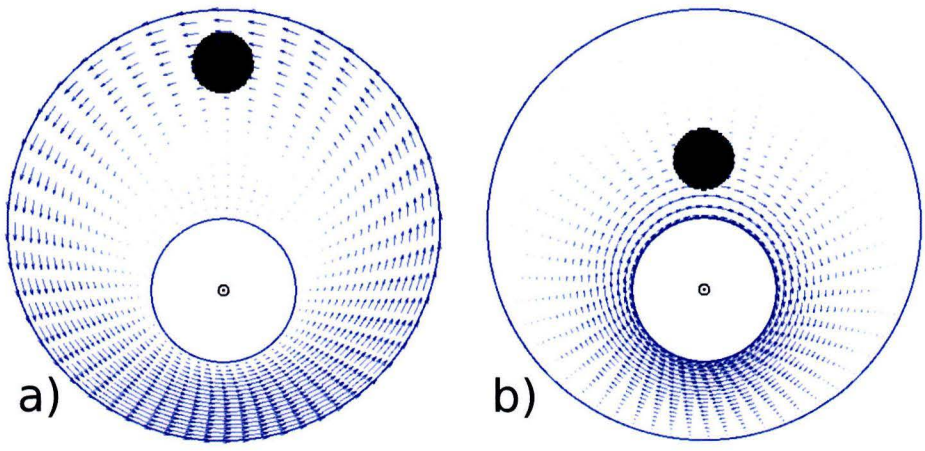


Figure C.2: Blob of dye overlaid by the vector field represented by the arrows corresponding to the flow created by first control input: (a) rotating the outer-cylinder; (b) rotating the inner-cylinder.

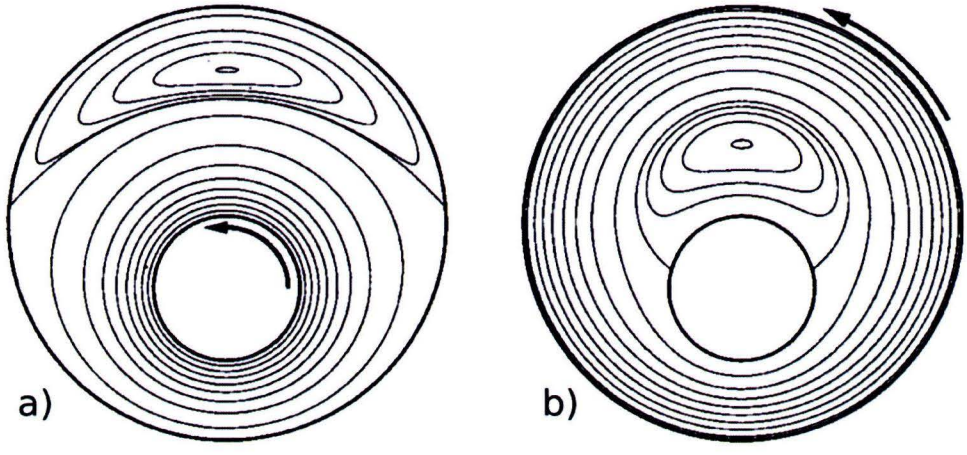


Figure C.3: Stream function of journal bearing flow: a) rotation of the inner cylinder, b) rotation of the outer cylinder. (source: [20])

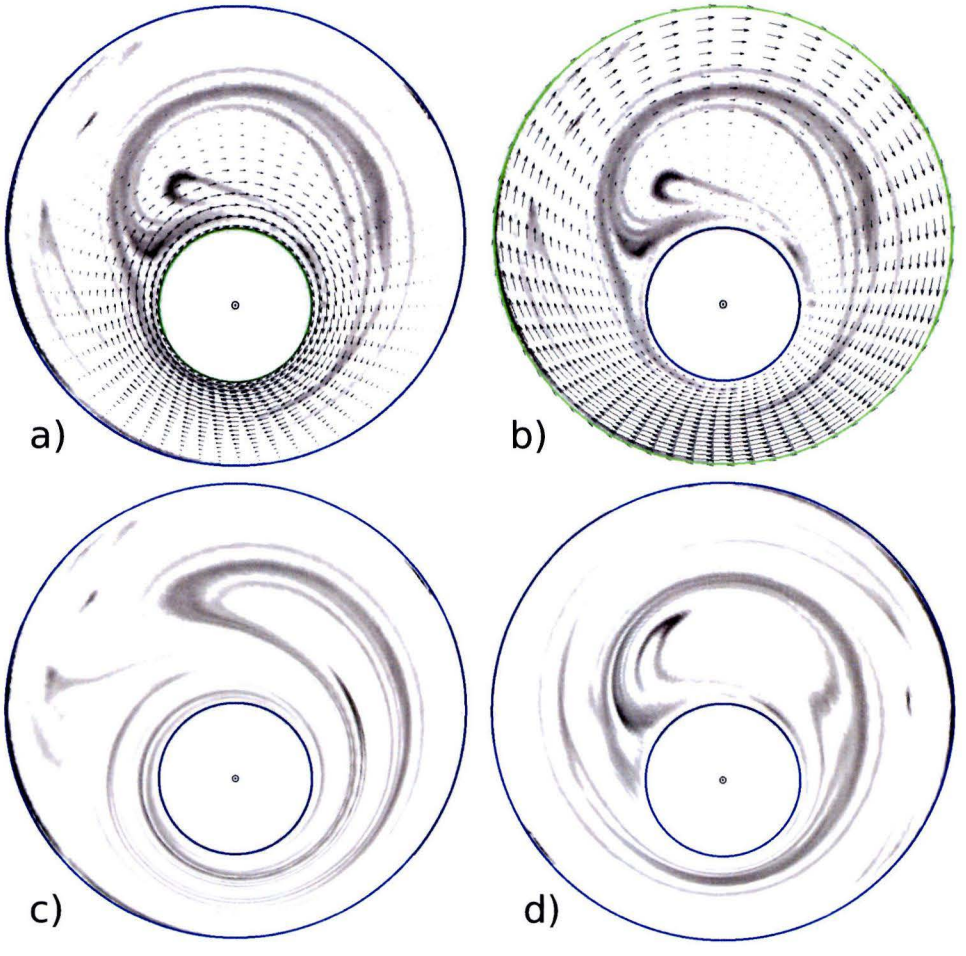


Figure C.4: Evolution of the dye for two different control actions. Figure a) and b) show an original measured scalar field with the velocity field overlaid corresponding to a clock-wise rotation of the inner cylinder and outer-cylinder respectively. Figure (c) and (d) show the predicted concentration field after a clockwise rotation of the inner and outer cylinder respectively. In the experiment, turning the inner-cylinder ((a) and (c)) is the chosen control input for this particular state.

clockwise rotation of the outer cylinder. Figure C.4(c) and Figure C.4(d) show the predicted concentration field after a clockwise rotation of the inner and outer cylinder respectively.

Before the measured state was captured, the last three actions were rotating the outer-cylinder for $\pi$[rad] (so $3\pi$ in total). For this reason, the concentration field starts to align with the vector field corresponding to the outer-cylinder movement as shown in Figure C.4(b). In the middle of the domain, an unmixed area has been formed. Important to notice is in FigureC.4(a) this region is overlapped by larger velocity gradients than Figure C.4(b). Consequently, during the experiment which executed the policy proposed in Section 4, the controller decided to turn the inner cylinder which resulted in the state given by Figure C.4(c). If the other control actions would have been chosen, the outer-cylinder would have stretched the dye further but would not have resolved the unmixed region as shown in Figure C.4(d). Hence ,the chosen action is in line with folding the stretched dye and is therefore an obvious choice. The controller reacts to relatively large spatial structures in the flow domain and therefore prevents island to occur.

# D Control horizon

In this section, more depth is given on how to choose the control horizon $k_F$. For the sake of clarity, the general mixing process is discussed in this section in order to reveal which the role of feedback. In a Stokes flow, the general mixing process can roughly be divided into three stages (shown in figure D.1). For an open-loop protocol, the mixing quality in the first stage is determined by the initial condition in particular. The system is sensitive to small perturbations, i.e. a small change in initial condition can yield very different mixing qualities (as shown in Figure 5.5). Hence, an advantage of feedback control is that it anticipates which makes the system less sensitive to perturbations in initial condition. The mixing performance in the second stage is mainly determined by the mixing protocol since at this point, the decrease in characteristic length scale is responsible for effective mixing. Hence, the role of feedback is important at this stage. At the last stage, the remaining features (such as islands) are being diminished by diffusion in particular. The slope of the intensity of segregation at this point is determined by the diffusion rate. Figure D.1 shows that this stage starts approximately after 30 steps. In case of the journal bearing flow, the control horizon is therefore chosen as $k_F = 30$.

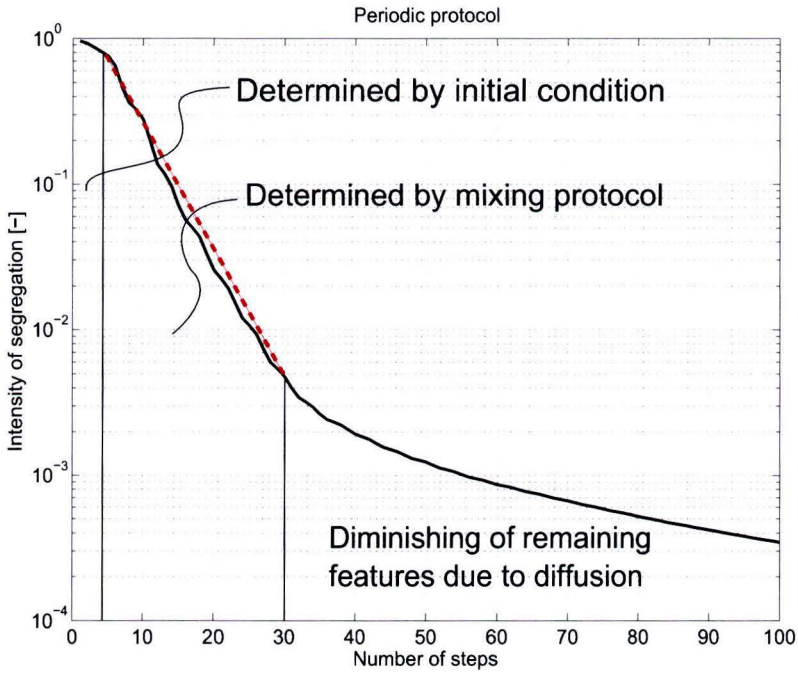


Figure D.1: General description of the mixing process

# E Mapping grid and diffusivity

The discretization of the domain, which is required for the mapping matrix method, introduces numerical errors due to the sub-domain averaging as shown in Section 3.1. Although the mapping matrices are derived for pure advective flow ($Pe \to \infty$) in this work, the numerical error causes artificial diffusion. Hence the error is often referred as numerical diffusion. Due to this diffusion, the mapping method might even be a better representation of reality as long as the numerical diffusivity mimics the real molecular diffusivity.

Gorodetskyi *et al.* [23, 24] studies the effects of numerical diffusion and shows that a quantitative correspondence between the spectral structure of the purely convective mapping matrix and that of the continuum advection-diffustion operator can be defined by means of an effective Péclet number. This effective Péclet number is proportional to the square of the linear grid size. However, the numerical diffusion only approximates the real diffusion since the effect of numerical diffusion and physical diffusion is not completely the same. For this reason, they show that the effects of molecular diffusion can be included into the mapping matrix formalism as well.

Interesting questions emerge from these statements with respect to controller design: (i) How fine to choose the mapping grid? (ii) Whether or not to include the molecular diffusion. In this Section, we analyze the influence of model diffusivity on control performance by means of simulations. Hereby, we investigate two cases: (i) the controller model diffusivity is smaller then the plant model diffusivity; (ii) the controller model diffusivity is larger than the plant model diffusivity.

## E.1 Simulations with diffusivity mismatch

The performance of the rollout algorithm can be influenced by the fact that often the (numerical) diffusion of the mapping matrices does not correspond to the actual molecular diffusion. So far, we solely considered mapping matrices based on pure advection (no diffusion). However as mentioned, the use of the mapping method introduces numerical diffusion. In order to study the effect of diffusion without the need to compute new mapping matrices, we used coarser grid in order to introduce more (numerical) diffusion.

The coarser mapping matrices can be derived from the mapping matrix $\Phi$ of $n_a \times n_r$ by merging groups of grid cells. Let $N$ be the number of cells being merged in tangential direction and $M$ the number cells being merged in radial direction. Using this method, the number of grid cells has been reduced from $n_a \times n_r$ to $n_a/N \times n_r/M$. Let $\mathbf{v}_i \subset \mathbb{N}^{N\times M}$ denote the vector corresponding to the $i$th grid cell of the reduced mapping matrix corresponding to $N \times M$ original grid cells being merged. The area of the $i$th reduced grid cell is denoted by $\Omega_i^r$ and the area the $i$th original grid cell by $\Omega_i^0$ such that

$$\Omega_i^r = \sum_{k=1}^{N\times M} \Omega^0_{\mathbf{v}_i(k)}.$$

Algorithm 3 shows how to compute the reduced mapping matrix.

**Algorithm 3** Algorithm for reducing mapping matrix

for $i = 1 : N \times M$

$\sigma^c_{\mathbf{v}_i} = \left[ \sum_{k=1}^{N\times M} \Phi_{\mathbf{v}_i(k)1} \quad \sum_{k=1}^{N\times M} \Phi_{\mathbf{v}_i(k)2} \quad \cdots \quad \sum_{k=1}^{N\times M} \Phi_{\mathbf{v}_i(k)n_a\times n_r-1} \quad \sum_{k=1}^{N\times M} \Phi_{\mathbf{v}_i(k)n_a\times n_r} \right]$
(vectors of column sums)

for $j = 1 : N \times M$

$\Omega^0_{\mathbf{v}_j} = \left[ \Omega^0_{\mathbf{v}_j(1)} \quad \Omega^0_{\mathbf{v}_j(2)} \quad \cdots \quad \Omega^0_{\mathbf{v}_j(N\times M-1)} \quad \Omega^0_{\mathbf{v}_j(N\times M)} \right]$

$\Omega^r_j = \sum_{k=1}^{N\times M} \Omega^0_{\mathbf{v}_j}(k)$

$\Phi^r_{ij} = \sum_{k=1}^{N\times M} \sigma^c_{\mathbf{v}_i}(\mathbf{v}_j(k))\Omega^0_{\mathbf{v}_j}(k)/\Omega^r_i$

end

end

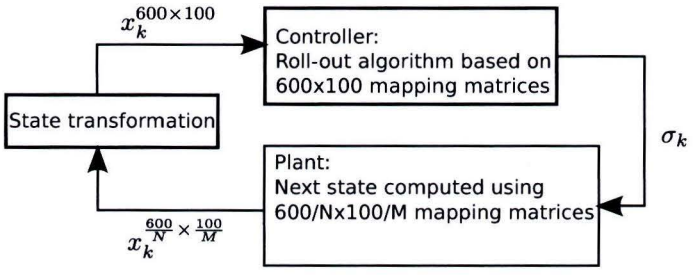


Figure E.1: Control diagram in case controller model diffusivity is smaller than the plant model diffusivity

At first, we investigate the case whereby the model diffusivity is smaller than the plant model diffusivity. Three policies were simulated for several grid sizes: (i) the periodic policy which is used as base policy for the rollout algorithm; (ii) The rollout policy in case the model used for the control algorithm exactly coincides with the plant model, i.e. the controller model and plant model have the same diffusivity; (iii) The rollout policy where the model diffusivity is smaller than the plant diffusivity. In the latter case, the controller uses mapping matrices based on the (full) grid of 600x100 but the evolution of the plant is determined by mapping matrices based on a coarser grid (as illustrated in Figure E.1). The result is presented in Figure E.2. Notice that a larger diffusivity enhances the homogenization rate, therefore simulations with coarser grids yield smaller intensity of segregations. In all cases, the diffusivity mismatch degraded the mixing performance. For the cases $N = 4; M = 4$ and $N = 8; M = 4$, the rollout policy performs even worse than the periodic protocol in despite of the closed-loop approach.

In order to examine the role of feedback with respect to a diffusivity mismatch, the open-loop behavior is shown in Figure E.3. Hereby, a sequence of control actions is determined on forehand via the rollout algorithm with a controller model based on the full grid and then applied to a plant model based on a coarser grid. By comparing Figure E.2 and Figure E.3, we can conclude that there is no significant difference is observable between the open-loop and closed-loop rollout thus in case the controller model diffusivity is smaller. Hence, feedback has no significant role with respect to such a diffusivity mismatch.

Secondly, we investigate the case whereby the controller model diffusivity is larger than the plant model diffusivity. Three policies were simulated the full grid of 600x100: (i) the periodic policy which is used as base policy for the rollout algorithm; (ii) The rollout policy whereby the controller model diffusivity exactly coincides with the plant model diffusivity; (iii) The rollout policy where the controller model diffusivity is larger than the plant model diffusivity. For the latter case, several controller model diffusivities were examined by using several coarser grids (as illustrated in Figure E.4). The results to these simulations are shown in Figure E.5. In all four cases, the performance of the first two policies should be the same since in all four case the same plant model is considered. The performance of the third policy is degraded due to the diffusivity mismatch as shown in Figure E.5. However, the rollout policy still outperforms the periodic protocol even for the case $N = 8; M = 4$. In order to examine the role of feedback with such a model mismatch, the results of the open-loop rollout policy are plotted in Figure E.6. Even in open-loop, all four cases outperform the periodic protocol. For the cases $N = 2; M = 2$ and $N = 4; M = 2$ the open-loop performance is close to the closed-loop. For the cases $N = 4; M = 4$ and $N = 8; M = 4$ however, a clear difference is visible. In case $N = 4; M = 4$, the open-loop case is better which can be explained by the fact that sub-optimal solutions are found. Hence, it can occur that the open-loop rollout policy performs better than the closed-loop policy. For the case $N = 8; M = 4$ the closed-loop rollout policy is the best. Given these observations, it is not possible to draw conclusions about the role of feedback in case the controller model diffusivity is larger than the plant model diffusivity.

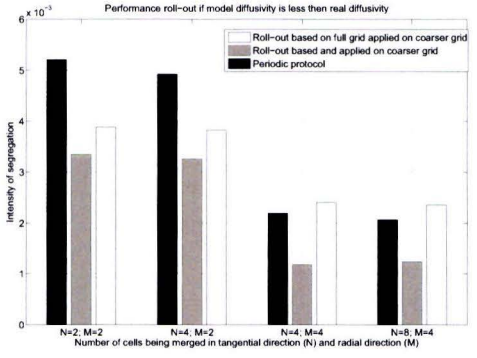


Figure E.2: Performance of the rollout policy (see Section 4) in terms of intensity of segregation after 30 steps in case the controller model diffusivity is smaller than the plant model diffusivity. In this figure, the periodic protocol (represented by the black bar) and the two rollout policies are evaluated by means of four different plant models based on the reduced grid of 600/Nx100/M. The gray bar represents the rollout policy whereby the controller models exactly coincide with the plant models. Hence they are based on the reduced grid of 600/Nx100/M. The white bars correspond to the rollout policy whereby there is a mismatch in diffusivity between the two models namely, the controller model is in all cases based on the full grid of 600x100. In case of such a diffusivity mismatch between the two models, the rollout policy does not always outperform its base policy.

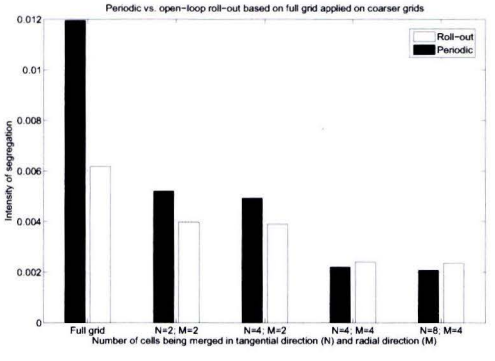


Figure E.3: Performance of the open-loop rollout policy (see Section 4)in terms of intensity of segregation after 30 steps in case the model diffusivity is smaller than the real diffusivity. In this figure, the periodic protocol (represented by the black bar) and the open-loop rollout policy (represented by the white bar) are evaluated by means of four different plant models based on the reduced grid of 600/Nx100/M. The mixing protocol corresponding to the open-loop rollout policy is determined *a priori* by means of the model based on the full grid of 600x100.

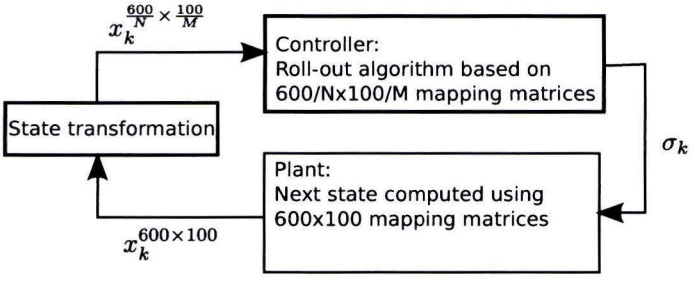


Figure E.4: Control diagram in case model diffusivity is larger than the plant diffusivity

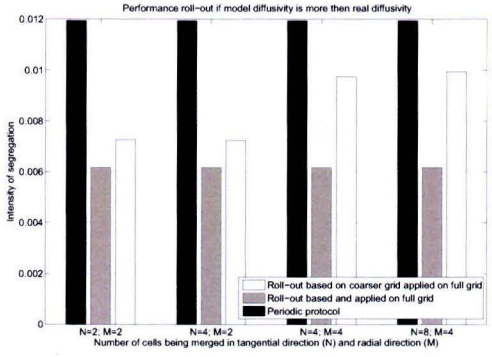


Figure E.5: Performance of the closed-loop rollout policy (see Section 4) in terms of intensity of segregation after 30 steps in case the model diffusivity is larger than the real diffusivity. In this figure, the periodic protocol (represented by the black bar) and the two rollout policies are evaluated by means of one plant models based on the full grid of 600x100. The gray bar represents the rollout policy whereby the controller models exactly coincide with the plant models. Hence they are based on the full grid of 600x100. Since the plant model is the same in all four cases, the results of the periodic protocol and the rollout policy represented by the gray bar are exactly the same. The white bars correspond to the rollout policy whereby there is a mismatch in diffusivity between the two models namely, the controller model is based on the reduced grid of 600/Nx100/M. In case of this diffusivity mismatch between the two models, the rollout policy still outperform its base policy. However, the diffusivity mismatch does degrade the performance.

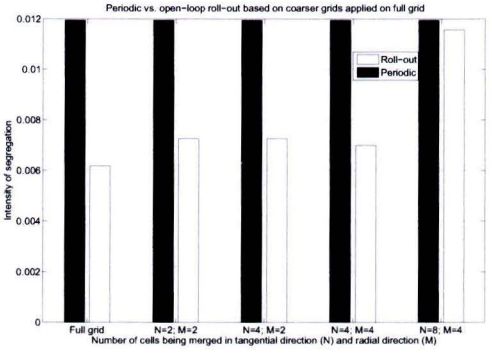


Figure E.6: Performance of the open-loop rollout policy (see Section 4) in terms of intensity of segregation after 30 steps in case the model diffusivity is larger than the real diffusivity. In this figure, the periodic protocol (represented by the black bar) and the open-loop rollout policy (represented by the white bar) are evaluated by means one plant model based on the full grid of 600x100. The mixing protocol corresponding to the open-loop rollout policy are determined *a priori* by means of model based on reduced grids of 600/Nx100/M.

## E.2 Conclusions and discussion

The results presented in Section E.1 showed that in general, a diffusivity mismatch the open-loop and closed-loop degrades the performance of the rollout algorithm. Furthermore, feedback has not shown a significant role with respect to a diffusivity mismatch. Therefore, it is recommended to incorporate molecular diffusion if present into the controller model in stead of using a model which assumes pure advection. In case computational resources are limited, it is not always possible to use an accurate model. In that case, a model with a coarser grid has to be used. However, the system is less affected in case the diffusivity of the model is larger than the case the model's diffusivity is smaller than the diffusivity of the plant. Moreover, using a coarser grid emphasizes the most dominant modes since the eigenvalue spectrum contracts to the origin [23, 24] which makes the system less sensitive to measurement noise.

# F Extensive description experiment

## F.1 Hardware

### F.1.1 Journal Bearing

As mentioned, the journal bearing flow is a flow within two eccentric cylinders. The experimental realization of this setup should meet two requirements. The setup should be able to rotate both cylinders independently where it is favorable to be able to adjust the velocity wave form. Secondly, it must be possible to be observe the entire domain without any obstructions and with a plain background.

A photo of the system is shown in Figure 5.2. The inner cylinder is solid rod of diameter 25 mm and length mm and the outer cylinder a transparent tube of inner diameter 75 mm and length mm which is sealed at the bottom edge with a transparent plate. The cylinders are driven by two identical Maxon servo motors (type A-max) connected to encoders (HEDL 5540, 500 counts per turn) for feedback control. The inner cylinder is directly connected to the gear. The outer cylinder is connected with the motor via a belt which is attached to a ring carrying the outer cylinder. In this way, the view from beneath is unobscured and the outer cylinder can easily be removed for cleaning. Note that it is not possible to avoid obstructions in the top-view because of frame which fixates inner cylinder. The mirror underneath the setup assures that there is sufficient space for the camera in front.

### F.1.2 E-box

The two servo motors are controlled via data-acquisition device, called the E-box. This device has two analog in- and outputs with a range of +/-10V, two encoder inputs and one digital in- and output which can be read/controlled by an external computer in real-time. Hence, in closed applications, the real-time code is executed by the external computer, i.e. the computer is part of the real-time loop. In our case, each of the two analog outputs are connected with an amplifier with an input range of +/-2.5V required for the servo motors.

### F.1.3 Camera

The most important requirements for the camera are that the resolution should be sufficient and the camera should be compatible with the OpenCV library discussed in Section F.2.2. The list of compatible camera's can be found here: http://opencv.willowgarage.com/wiki/Welcome/OS. Be aware that not all compatible camera's are listed on this page. Most camera's which compatible with V4L2 (a video capture application programming interface for Linux), are also compatible with OpenCV. Furthermore, a large focal length is desired which will be discussed in Section H.4. In this work, a Logitech HD Webcam C525 http://www.logitech.com/nl-nl/product/hd-webcam-c525?crid=34 is used. The camera is connected via USB.

The camera should be aligned with the setup. However, the distance is not important as long as it captures whole the domain since software is programmed such that the region of interest can easily be adjusted.

## F.2 Software

### F.2.1 Ubuntu

As mentioned in Section F.1.2, the external computer is part of the control loop. Therefore the computer should process data without buffering delays. This can be managed by using a real-time operating system (RTOS). For this research, such an operating system should also support Matlab/Simulink and OpenCV. Ubuntu is a free open source easy to use operating system which is compatible with these applications. The standard installation of Ubuntu is not a RTOS but the kernel, the component of an operating system which manages the system resources, can be customized such that it supports real-time applications. The easiest way to install this system is via the wubi-installer can be obtained from the TU/e network share: \\ai-stosrv02\EBox. This installer

copies an image where Matlab/Simulink is already installed including the required code for the E-box. More details like how to activate Matlab and configure the correct Ethernet port can be found here: http://cstwiki.wtb.tue.nl/index.php?title=E-box.

### F.2.2 OpenCV

OpenCV (Open Source Computer Vision) is a library of programming functions for real time computer vision. This library contains several image processing functions for among other C++. Using this library, we are able to program are own Simulink blocks which can incorporate and process the webcam data. The default image processing blocks of Matlab/Simulink are not supported by the real-time code generator of Matlab. Make sure to install OpenCV according to the following guide: http://opencv.willowgarage.com/wiki/InstallGuide#. Be aware that it is necessary to install the following packages during step 2 for video capturing: ffmpeg, libgstreamer, libv4l, libxine, unicap, libdc1394 2.x. The most important commando's for this application are:

- `cvCreateCameraCapture` for initializing the camera.
- `cvSetCaptureProperty` for defining the camera's resolution.
- `cvQueryFrame` to obtain a frame/image.
- `cvtColor` to convert RGB to other color spaces.

### F.2.3 Matlab/Simulink

Matlab/Simulink is an easy environment to build up a control scheme. Via a S-function block, it is possible to write a function in C++ which is compatible with Simulink. This is required in order to be able to take camera frames and controlling the maxon motors simultaneously. In our case, this function is defined as follows; The block can be triggered via an external signal. After the block is triggered, it captures and processes an image from the webcam and computes the next desired mixing action according to the algorithm proposed in Part II. If the computations are not finished yet, the trigger signal is being ignored. The entire C-code of this S-function is rather tedious to present in this report, hence only essential commando's will be briefly elucidated.

The sparse mapping matrices to predict the fluids behavior were provided as mat-file containing variables which can be read by matlab. The library to read these variables in C-code is not supported by the real-time code generation. Therefore, the mat-files first have to be converted to text files by the stand-alone C-code convertmatfiles.cpp. A sparse matrix is represented by three vectors; one vector $i_r$ which represents the rows with non-zero elements, one vector $i_c$ which represents the column with non-zero elements and one vector $p_r$ with the values of the non-zero elements. Note that these three vectors are sufficient to reconstruct the corresponding full matrix. The following commando's are used for the conversion:

- `matOpen` to load the mat-file.
- `matGetNextVariable` to store the content to a C-variable of type mxArray.
- `matClose` to close the mat-file.
- `mxGetIr` to obtain vector $i_r$.
- `mxGetJc` to obtain vector $i_c$.
- `mxGetPr` to obtain vector $p_r$.
- `mxGetNzmax` to obtain the number of non-zero elements.
- `ofstream` to create a data stream in order to write a text file.

The code to build and run convertmatfiles.cpp is include in the m-file buildcapture.m.

### F.2.4 How to start an experiment

At first, make sure that the setup is covered by the white cloth in order to prevent glares on the image. Furthermore, the camera should be placed in front of a dark background in order to avoid undesired reflections in the mirror. After the setup is connected properly as explained in Section F.1, the experiment can be started by running run.m. At first, the code will ask to build all the files which is necessary to create stand-alone executables. Press yes if any changes are made in the code else press no in order to skip the building procedure. After this step, the code will request an experiment name. The code will create a folder with this name to store the experiment's output. Make sure that this name does not include a space.

Now, the transparent bin can be filled with polymer. It is recommended to fill the bin with a polymer layer (without dye) of at least 2 cm thick in order to exclude bottom effects. Let the polymer rest for a while in order to release the air bubbles. One could place the bin into a vacuum vessel to accelerate this process.

The camera calibration is required for selecting the region of interest. Although algorithms exist to recognize circular figures (like the hough transform), they are not as accurate as selecting them manually. Subsequently, the dye/contrast fluid should be dropped. The screen will show the live camera image including a small circle where the dye should be dropped. In this way, the dye can approximately be dropped at the same location each experiment. At last, real-time code of the Simulink scheme will be executed. The output screen shows the progress of the experiment. After approximately 10 minutes, the experiment is finished.

# G Vision

## G.1 Saturation threshold

In order to filter out the plain background from the image, a threshold has to be defined. In despite of the fact the the dye is darker then the background, the gray scale is not a suitable measure. The gray-scale is sensitive to shades and gray values of the dye and background can be close to each other. Hence, it is better to use the fact that the dye is colored. The saturation refers to the perceived intensity of a color (see figure G.1b). Therefore, a clear difference in saturation is noticeable as shown in figure G.1a. This saturation can be obtained by transforming the RGB (red, green and blue intensities) value into HSL (hue, saturation and lightness) values. Note that the solved pigment used as dye shouldn't be to dark in order to obtain a visible measurable in saturation.

The conversion of RGB to HSL is given by:

$$
\begin{aligned}
R' &= R/255 \\
G' &= G/255 \\
B' &= B/255 \\
C_{max} &= \max(R', G', B') \\
C_{min} &= \min(R', G', B') \\
\Delta &= C_{max} - C_{min} \\
H &= \begin{cases} \frac{\pi}{3}\left(\frac{G'-B'}{\Delta}\right) \bmod 6 & , C_{max} = R' \\ \frac{\pi}{3}\left(\frac{B'-R'}{\Delta} + 2\right) & , C_{max} = G' \\ \frac{\pi}{3}\left(\frac{R'-G'}{\Delta} + 4\right) & , C_{max} = B' \end{cases} \\
S &= \begin{cases} 0 & , \Delta = 0 \\ \frac{\Delta}{1-|2L-1|} & , \Delta \neq 0 \end{cases}
\end{aligned}
$$

(a) Measured saturation

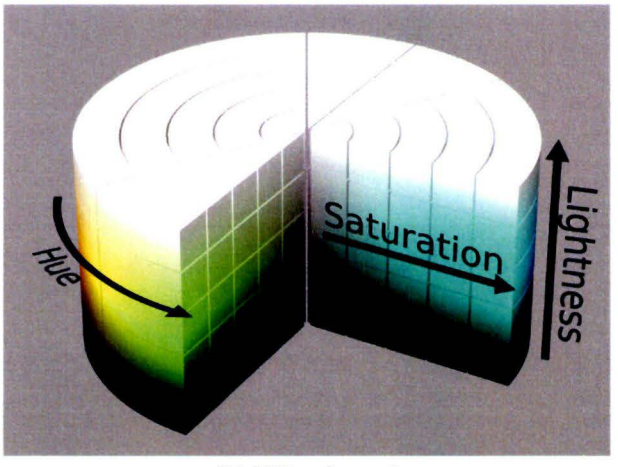


(b) HSL color scale

## G.2 Averaging pixel values

In order to reduce the effect of measurements noise, the value of a grid cell is based on the average of all pixels within that grid cell. Furthermore, using averaging, less data will get lost due to a threshold. In this case the grid is chosen such that a the cell boundary consist of two straight lines and two circular line segments (shown in figure G.1). However, if the number of cells is chosen sufficient large, the

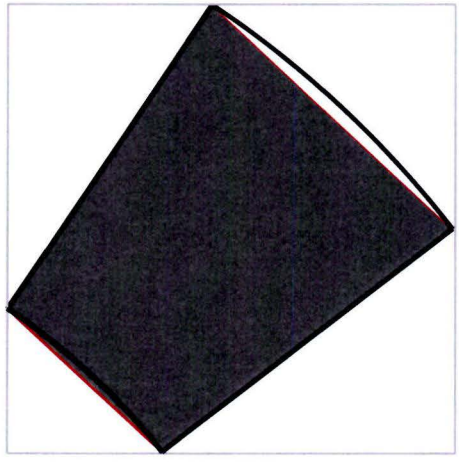

Figure G.1: The pixels with the filled quadrature are used for averaging.

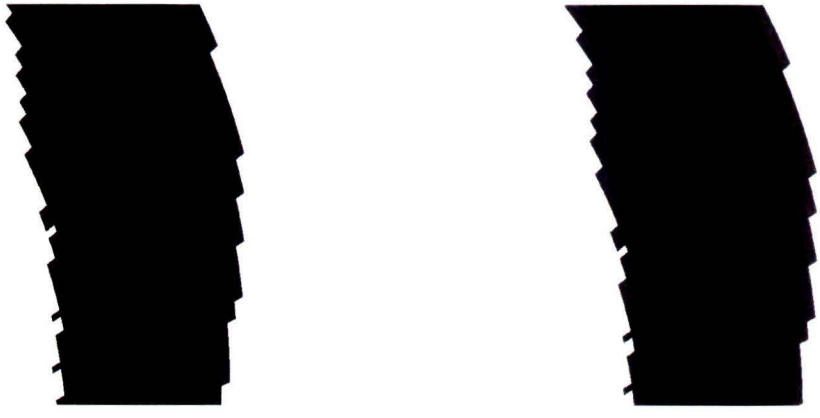

a) b)

Figure G.2: Result of averaging on a measured state: a) before averaging, b) after averaging. Note that these two figures are zoomed on a part of the flow domain. Note that the image of the state after averaging looks more smooth. Hence the effect of measurement noise has been reduced.

circular line segments are nearly straight. Therefore, to ease computations, we assume that each grid cell is approximately quadrangular where the vertices coincide with the actual grid cell shape. The grid cell can now be described by four linear functions which eases the search for pixels within the cell. In order to check which pixels lie within this quadrangle efficiently, only the pixels within a rectangular which encloses the grid cell are considered. The result is shown in figure G.2.

# H Error Analysis Experiment

Several experiments were executed. At first to verify the mapping method. Since the flow is dominated by viscous forces ($Re << 1$) and we are dealing with a Newtonian fluid, the analytical velocity field given by [54] is a reliable representation of the fluids behavior, as confirmed in several papers [50, 31]. Therefore, we can expect that the mapping method is an accurate representation of the fluid behavior. However, the predictions according to the model do not match the experiments. Since model is assumed to be correct, measurement errors are responsible for the mismatch. This Section discusses potential causes for these measurement errors.

## H.1 Beer-Lambert law

Before, we assumed the luminosity is proportional to the concentration. However, the actual relation between luminosity and concentration is given by the Beer-Lambert law:

$$\epsilon c d = -\log\left(\frac{I}{I_0}\right) \tag{H.1}$$

where $I_0$ is the original luminosity, $I$ the measured luminosity, $\epsilon$ the extinction coefficient and $d$ the path length. If the measured luminosity of the mixture is the same as the original, all light has been passed through the fluid and therefore the concentration is zero. If $I = 0$, no light has been passed. In order to examine how this measurement error affects the performance of the rollout policy, several simulations have been executed where

$$C_{measure} = 1 - 10^{\alpha C_{real}} \frac{M_0}{M_{real}}, \quad \alpha = \{\frac{1}{2}, 1, 2, 3, 4, 5\}. \tag{H.2}$$

and where $\frac{M_0}{M_{real}}$ is chosen such that the mass remains preserved. Note that H.2 is based on (H.1) where $C_{measure} = 1 - \frac{I}{I_0}$. This relation is plotted in Figure H.1. The results plotted in Figure H.2 and H.3. The effect of the non-linear relation given by (H.2) appears to be not significant. This can be explained by the fact that relation (H.2) is approximately linear for small $C_{real}$.

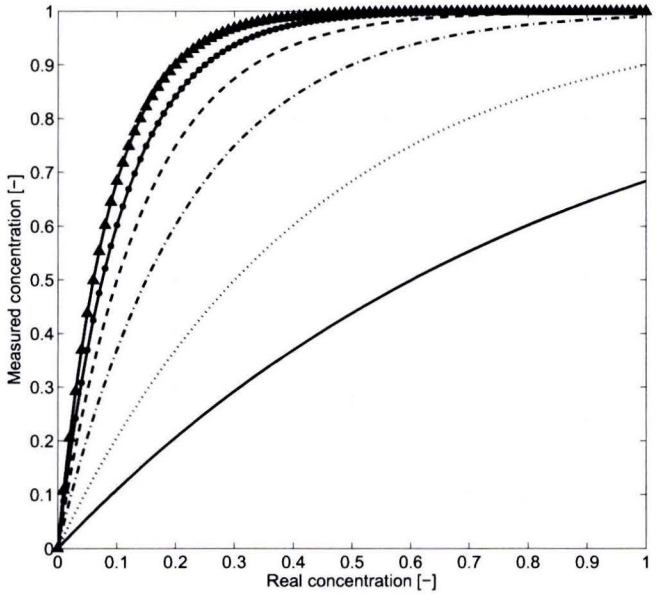


Figure H.1: Evaluated non-linear functions between real concentration and measured concentration.

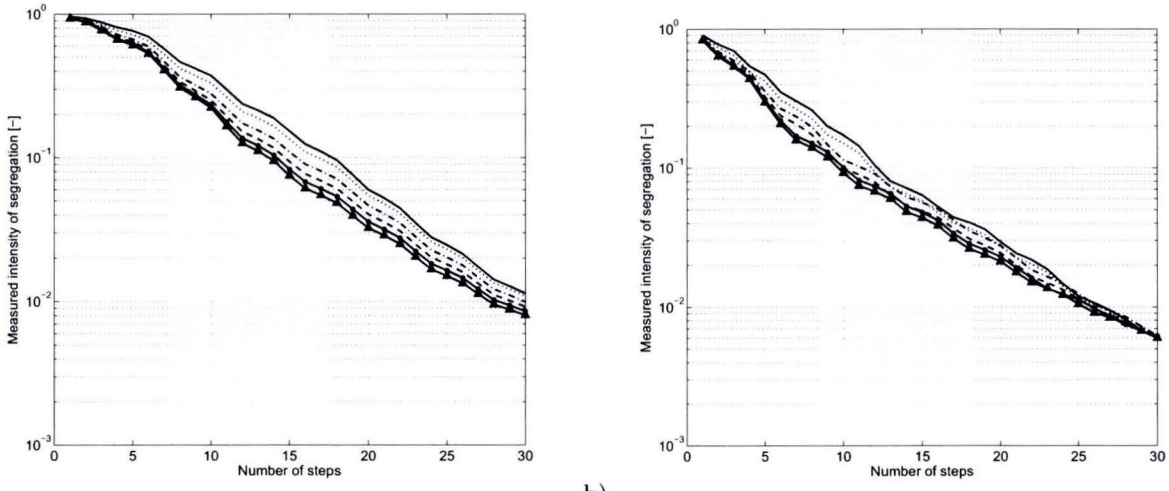


a) b)

Figure H.2: Result of simulations based on the non linear relations shown in figure H.1. a) uses a periodic policy and b) a rollout policy which actions are based on the measured intensity of segregation.

## H.2 Quantization

The OpenCV library used for the experiments is limited to 8-bit images which means the color is distributed over 256 bins. The images captured in the experiments only use a subset of this spectrum though. The influence of quantization is determined by simulating the periodic policy whereby the measured state has been quantized and scaled such that the mass preserving property is still maintained. The result is shown in figure H.4. The initial are not significantly affected by the quantization. The quantization starts to play role as the mixture homogenizes which is visible for $N = 10$ in particular. The quantization does influence the result but not significantly if a sufficient number of bins is chosen.

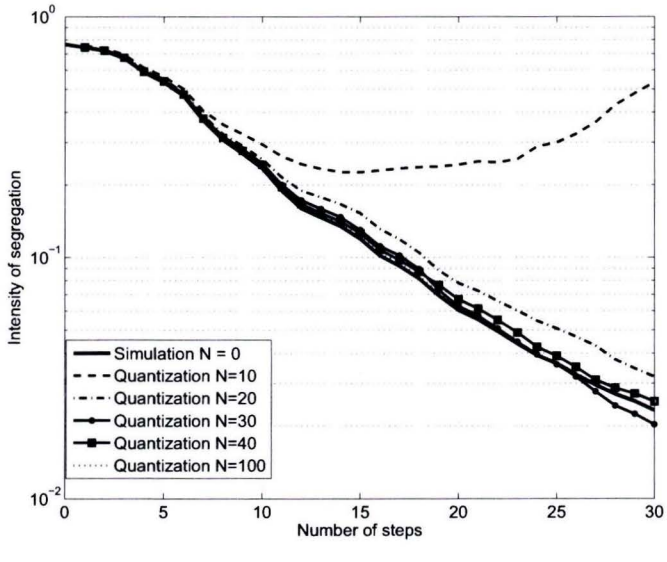


Figure H.4: Simulation with quantization. $N$ is the number of bins used for quantization.

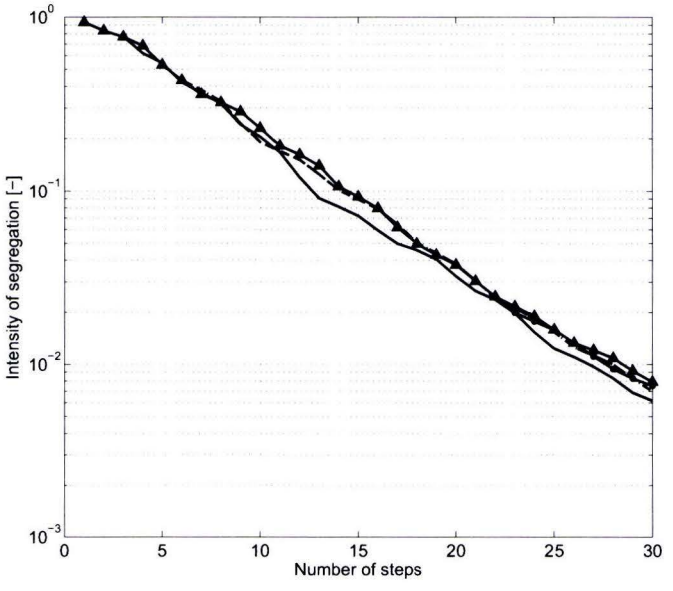


Figure H.3: Intensity of segregation based on real concentration.

## H.3 Diffusion

As mentioned in Section E, in general a mismatch in diffusivity degrades the performance of the rollout policy. Hence, a better performance can be expected if the model diffusivity is a good representation of the actual diffusivity. Figure H.5 shows a comparison between experiment and simulation whereby models with a grid of 600x100 and a grid of 300x50 were used. Figure H.6 shows the intensity of segregation determined in both experiment and simulation. Although the full matrix appears to be the best representation in terms of intensity of segregation based on Figure H.6, Figure H.5 shows that the numerical diffusion corresponding to the grid of 300x50 better match the actual diffusion since the striations are more blurred as in the experiment.

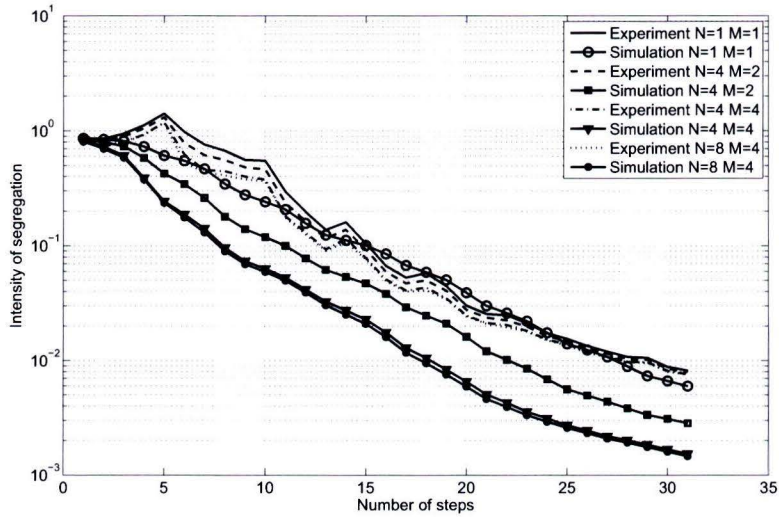


Figure H.6: Intensity of segregation of experiment compared to simulation mapping matrices with different grid sizes. Note that with a coarser grid the intensity of segregation of the simulation decreases due to sub-domain averaging (3.4). Based on this figure, the finest grid appears to be the best representation in terms of intensity of segregation. However, one cannot say whether other measurement errors play role as well.

Figure H.5: Experiment (left) compared to simulation (right) using a 600x100 mapping matrix (upper row) and a 300x50 mapping matrix (lower row). Based on this figure, the mapping matrix of 300x50 shows a better correspondence with the measured state due to the presence of diffusion in the experiments.

## H.4 Camera perspective

Due to the finite focal length, the edge of the outer cylinder will always be visible as illustrated in figure H.7. To overcome this problem, one can increase the distance between the camera and the object and zoom into the object. However, if the zoom is digital, high resolution pictures are required. Another option is to place a (biconvex) lens in between the camera and the object or to use a tele photo camera lens.

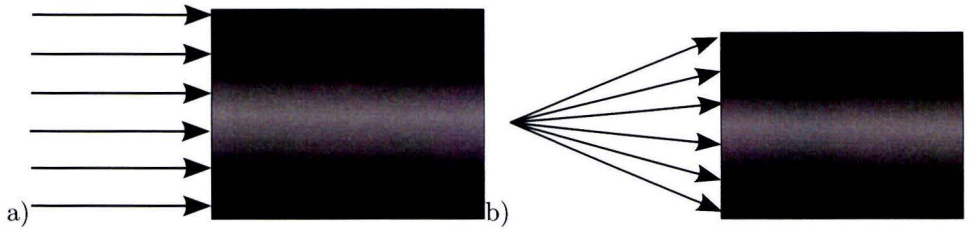


Figure H.7: Observation of camera: a) the ideal case, b)

# References


[1] O.M. Aamo, M. Krstic, and T.R. Bewley. Control of mixing by boundary feedback in 2D channel flow. *Automatica*, 39(9):1597 – 1606, 2003.

[2] K.T. Alligood, T. Sauer, and J.A. Yorke. *Chaos : an introduction to dynamical systems*. Textbooks in mathematical sciences. Springer, New York, 1996.

[3] D.J. Antunes, W.P.M.H. Heemels, J.P. Hespanha, and C.J. Silvestre. Scheduling measurements and controls over networks - part i: Rollout strategies for protocol design. In *American Control Conference (ACC), 2012*, Jun. 2012.

[4] D.J. Antunes, W.P.M.H. Heemels, J.P. Hespanha, and C.J. Silvestre. Scheduling measurements and controls over networks - part ii: Rollout strategies for simultaneous protocol and controller design. In *American Control Conference (ACC), 2012*, Jun. 2012.

[5] H. Aref. Stirring by chaotic advection. *Journal of Fluid Mechanics*, 143:1–21, 5 1984.

[6] G. K. Batchelor. *An Introduction to Fluid Dynamics*. February 2000.

[7] R.E. Bellman. *Dynamic Programming*. Dover Books on Computer Science Series. Dover Publications, Incorporated, 2003.

[8] D.P. Bertesekas. *Dynamic Programming and Optimal Control*. Arthena Scientific, 2005.

[9] J.H.E. Cartwright, M. Feingold, and O. Piro. An introduction to chaotic advection. In H. Chaté, E. Villermaux, and J.M. Chomaz, editors, *Mixing*, volume 373 of *NATO ASI Series*, pages 307–342. Springer US, 1999.

[10] J. Chaiken, R. Chevray, M. Tabor, and Q. M. Tan. Experimental study of Lagrangian turbulence in a Stokes flow. *Proceedings of the Royal Society of London. A. Mathematical and Physical Sciences*, 408(1834):165–174, 1986.

[11] B.V. Chirikov. A universal instability of many-dimensional oscillator systems. *Physics Reports*, 52(5):263 – 379, 1979.

[12] L. Cortelezzi, A. Adrover, and M. Giona. Feasibility, efficiency and transportability of short-horizon optimal mixing protocols. *Journal of Fluid Mechanics*, 597:199–231, 1 2008.

[13] I. J. Couchman and E.C. Kerrigan. Control of mixing in a Stokes fluid flow. *Journal of Process Control*, 20(10):1103 – 1115, 2010.

[14] P.J. Cullen. *Food Mixing: Principles and Applications*. Wiley-Blackwell, 2009.

[15] D. D'Alessandro, M. Dahleh, and I. Mezic. Control of mixing in fluid flow: a maximum entropy approach. *Automatic Control, IEEE Transactions on*, 44(10):1852–1863, 1999.

[16] P.V. Danckwerts. The definition and measurement of some characteristics of mixtures. *Applied Scientific Research, Section A*, 3(4):279–296, 1952.

[17] G.S. Deaecto, A.R. Fioravanti, and J.C. Geromel. Suboptimal switching control consistency analysis for discrete-time switched linear systems. *European Journal of Control*, 19(3):214 – 219, 2013.

[18] S.M. Kresta E.L. Paul, V.A. Obeng. *Handbook of Industrial Mixing: Science and Practice*. John Wiley and Sons, 2003.

[19] J. G. Franjione, C-W. Leong, and J.M. Ottino. Symmetries within chaos: A route to effective mixing. *Physics of Fluids A: Fluid Dynamics*, 1(11):1772–1783, 1989.

[20] O.S. Galaktionov, P.D. Anderson, and Peters. Structure development during chaotic mixing in the journal bearing flow. *Phys. Fluids*, 14(9), 2002.

[21] J. C. Geromel and P. Colaneri. Stability and stabilization of discrete time switched systems. *International Journal of Control*, 79(7):719–728, 2006.

[22] J.C. Geromel, G.S. Deaecto, and J. Daafouz. Suboptimal switching control consistency analysis for switched linear systems. *IEEE Trans. Automat. Contr.*, 58(7):1857–1861, 2013.

[23] O. Gorodetskyi, M. Giona, and P.D. Anderson. Exploiting numerical diffusion to study transport and chaotic mixing for extremely large péclet values. *Europhys. Lett.*, 97:14002, 2012.

[24] O. Gorodetskyi, M. Giona, and P.D. Anderson. Spectral analysis of mixing in chaotic flows via the mapping matrix formalism - inclusion of molecular diffusion and quantitative eigenvalue estimate in the purely convective limit. *Phys. Fluids*, 24:073603, 2012.

[25] O. Gorodetskyi, M.F.M. Speetjens, and P.D. Anderson. An efficient approach for eigenmode analysis of transient distributive mixing by the mapping method. *Phys. Fluids*, 24(053602), 2012.

[26] W.P.M.H. Heemels, B. De Schutter, J. Lunze, and M. Lazar. Stability analysis and controller synthesis for hybrid dynamical systems. *Philosophical Transactions of the Royal Society A: Mathematical, Physical and Engineering Sciences*, 368(1930):4937–4960, 2010.

[27] M. Hoeijmakers, F. Fontenele Araujo, G. van Heijst, H. Nijmeijer, and R. Trieling. Control of mixing via entropy tracking. *Phys. Rev. E*, 81:066302, Jun 2010.

[28] C.L. Tucker III and G.W.M. Peters. Global measures of distributive mixing and their behavior in chaotic flows. *Korea-Aust Rheo J*, 4(15):197 208, 2003.

[29] T.G. Kang, M.K. Singh, T.H. Kwon, and P.D. Anderson. Chaotic mixing using periodic and aperiodic sequences of mixing protocols in a micromixer. *Microfluidics and nanofluidics*, 4(6):589–599, 2008.

[30] D. Kressner. Large periodic lyapunov equations: Algorithms and applications, 2003.

[31] P.G.M. Kruijt, O.S. Galaktionov, P.D. Anderson, G.W.M. Peters, and H.E.H. Meijer. Analyzing mixing in periodic flows by distribution matrices: Mapping method. *AIChE Journal*, 47(5):1005–1015, 2001.

[32] T. Li, Y. Fan, Y. Cheng, and J. Yang. An electrochemical lab-on-a-cd system for parallel whole blood analysis. *Lab on a Chip - Miniaturisation for Chemistry and Biology*, 13(13):2634–2640, 2013.

[33] D. Liberzon. *Switching in Systems and Control*. Systems and Control. Birkhäuser, 2003.

[34] M. Liu, F. J. Muzzio, and R. L. Peskin. Quantification of mixing in aperiodic chaotic flows. *Chaos, Solitons & Fractals*, 4(6):869–893, June 1994.

[35] J. Lunze and F. Lamnabhi-Lagarrigue. *Handbook of Hybrid Systems Control: Theory, Tools, Applications*. Cambridge University Press, 2009.

[36] G. Mathew, I. Mezic, S. Grivopoulos, U. Vaidya, and L. Petzold. Optimal control of mixing in Stokes fluid flows. *Journal of Fluid Mechanics*, 580:261–281, Jun 2007.

[37] G. Mathew, I. Mezic, and L. Petzold. A multiscale measure for mixing. *Physica D: Nonlinear Phenomena*, 211(1-2):23 – 46, 2005.

[38] M.F. Mora, A.M. Stockton, and P.A. Willis. Analysis of thiols by microchip capillary electrophoresis for in situ planetary investigations. *Electrophoresis*, 34(2):309–316, 2013.

[39] F.J. Muzzio, P.D. Swanson, and J.M. Ottino. The statistics of stretching and stirring in chaotic flows. *Phys. Fluids*, 3(822), 1991.

[40] J.M. Ottino. *The Kinematics of Mixing: Stretching, Chaos, and Transport*. Cambridge Texts in Applied Mathematics. Cambridge University Press, 1989.

[41] J.M. Ottino and S. Wiggins. Introduction: mixing in microfluidics. *Philosophical Transactions of the Royal Society A: Mathematical, Physical and Engineering Sciences*, 362(1818):923–935, May 2004.

[42] E. Fu K. Helton K. Nelson M.R. Tam Bernhard H. Weigl P. Yager, T. Edwards. Microfluidic diagnostic technologies for global public health. *Nature*, (7101):412–418, 2006.

[43] T.S. Parker and L.O. Chua. *Practical numerical algorithms for chaotic systems*. Springer Verlag, 1989.

[44] Y.B. Pesin. Characteristic Lyapunov exponents, and smooth ergodic theory. *Uspehi Mat. Nauk*, 32(4 (196)):55–112, 287, 1977.

[45] O. Reynolds. Study of fluid motion by means of coloured bands, 1894.

[46] Andrey V. Savkin and Robin J. Evans. *Hybrid Dynamical Systems: Controller and Sensor Switching Problems*. Springer-Verlag New York, Inc., Secaucus, NJ, USA, 2001.

[47] M.K. Singh, T.G. Kang, H.E.H. Meijer, and P.D. Anderson. The mapping method as a toolbox to analyze, design, and optimize micromixers. *Microfluidics and nanofluidics*, 5(3):313–325, 2008.

[48] M.K. Singh, M.F.M Speetjens, and P.D. Anderson. Eigenmode analysis of scalar transport in distributive mixing. *Phys. Fluids*, 21(093601), 2009.

[49] M.F.M. Speetjens, M. Lauret, H. Nijmeijer, and P.D. Anderson. Footprints of Lagrangian flow structures in eulerian concentration distributions in periodic mixing flows. *Physica D: Nonlinear Phenomena*, 250(0):20 – 33, 2013.

[50] P.D. Swanson and J. M. Ottino. A comparative computational and experimental study of chaotic mixing of viscous fluids. *Journal of Fluid Mechanics*, 213:227–249, 3 1990.

[51] V. M. Uhl and J. B. Gray. *Mixing theory and practice*. Number 4. Academic Press, New York, 1966.

[52] A. Varga and P. Van Dooren. Computational methods for periodic systems - an overview, 2001.

[53] Tucker W. Computing accurate Poincaré maps. *Physica D*, 171(3):127–137, 2002.

[54] G.H. Wannier. A contribution to the hydrodynamics of lubrication. *Quarterly of Applied Mathematics*, 8:1–32, 1950.

[55] S. Wiggins and J.M. Ottino. Foundations of chaotic mixing. *Phil. Trans. R. Soc. Lond.*, 362:937–970, 2004.

[56] W. Zhang, A. Abate, J. Hu, and M.P. Vitus. Exponential stabilization of discrete-time switched linear systems. *Automatica*, 45(11):2526 – 2536, 2009.

[57] W. Zhang, J. Hu, and A. Abate. On the value functions of the discrete-time switched LQR problem. *Automatic Control, IEEE Transactions on*, 54(11):2669–2674, 2009.

[58] W. Zhang, J. Hu, and A. Abate. Infinite horizon switched LQR problems in discrete time: A suboptimal algorithm with performance analysis. *IEEE Transactions on Automatic Control*, 57(7):1825–1821, 2012.

[59] Y. Zhao, D. Chen, H. Yue, J.B. French, J. Rufo, S.J. Benkovic, and T.J. Huang. Lab-on-a-chip technologies for single-molecule studies. *Lab on a Chip - Miniaturisation for Chemistry and Biology*, 13(12):2183–2198, 2013.